ORIGINAL PAPER

The behavior of Li and B isotopes in high-*T* and low-*T* eclogites enclosed by phengite schists

Dan Wang[1] · Rolf L. Romer[2] · Fulai Liu[1] · Johannes Glodny[2]

Abstract

Subduction zones are critical sites for recycling of Li and B into the mantle. The way of redistribution of Li and B and their isotopes in subduction settings is debated, and there is a lack of detailed studies on Li and B partitioning between minerals of different types of eclogites and the host rocks of the eclogites. We present Li and B concentration data of minerals and Li and B whole-rock isotope data for low-*T* and high-*T* eclogites and their phengite schist host rocks from the Changning–Menglian suture zone, SW China. Omphacite controls the Li budget in both the low-*T* and high-*T* eclogites. Low-*T* eclogites have Li and δ^7Li values (8.4–27.0 ppm, − 5.5 to + 3.2 ‰) similar to the phengite schists (8.7–27.0 ppm, − 3.8 to + 3.0 ‰), suggesting that Li was added to low-*T* eclogites from the phengite schists. In contrast, high-*T* eclogites have much lower δ^7Li values (− 13.2 to − 5.8 ‰) than the phengite schists, reflecting prograde loss of Li or exchange with wall rocks characterized by low δ^7Li values. Phengite and retrograde amphibole/muscovite are the major B hosts for low-*T* and high-*T* eclogites, respectively. The budgets and isotopic compositions of B in eclogites are affected by the infiltration of fluids derived from phengite schists, as indicated by eclogite δ^{11}B values (− 15.1 to − 8.1 ‰) overlapping with the values of the phengite schists (− 22.8 to − 9.5 ‰). Lithium and B in eclogites are hosted in different mineral phases that may have formed at different stages of metamorphism, implying that the contents and isotopic compositions of Li and B may become decoupled during subduction-related fluid-mediated redistribution. We suggest a mineralogical control on the redistribution of Li and B in eclogites during subduction and the exchange of Li and B with the immediate wall rocks. The observed contrasting Li and B isotopic signatures in eclogites are likely caused by a fluid-mediated exchange with different types of wall rocks during both prograde metamorphism and exhumation.

Introduction

Subduction of oceanic crust and its overlying sediments carries fluids into the mantle (Peacock et al. 1990; Plank and Langmuir 1993; Spandler et al. 2008; Zellmer et al. 2015). Fluids expelled during prograde metamorphism at higher temperatures and pressures from subducting slabs may fertilize the mantle above the slab (Foley 1992; Liu

et al. 2022; Prelević et al. 2012; Soder and Romer 2018). Partial melting of the metasomatized, veined mantle during the same or a later tectonic event and variable interaction of these melts with the ambient mantle and the crust eventually account for the diversity of arc magmatism and post-collisional alkaline rocks (Bebout and Barton 1989; Conticelli et al. 2009; Ishikawa and Nakamura 1994; Prelević et al. 2012; Soder and Romer 2018) that carry volatile components and fluid-mobile elements back to the crust.

Lithium and B are fluid-mobile elements that are lost from altered oceanic crust and sediments during subduction-related prograde metamorphism. This loss of Li and B from the oceanic crust and sediments results in lower δ^7Li and δ^{11}B values in the residue of the slab (Konrad-Schmolke and Halama 2014; Peacock and Hervig 1999; Wunder et al. 2005, 2007). However, eclogites and blueschists have a

✉ Dan Wang
  wangd221@gmail.com

[1] Institute of Geology, Chinese Academy of Geological Sciences, Beijing 100037, China

[2] GFZ German Research Centre for Geosciences, Telegrafenberg, 14473 Potsdam, Germany

large range in Li and B contents and isotopic compositions (Cannaò et al. 2023; John et al. 2012; Peacock and Hervig 1999; Marschall et al. 2007a, b; Zack et al. 2003), which is not caused by fractionation during prograde subduction alone (Marschall et al. 2007b). Phase transformation is commonly accompanied by redistribution of Li and B. The stability of Li and B hosting mineral phases controls the gain or loss history of the different lithologies of the subducting slab (Romer and Meixner 2014; Marschall et al. 2007b). Furthermore, different minerals (e.g. smectite, chlorite, illite, sericite) have contrasting potentials to sequester Li and B, which may decouple both the fractionation and mobilization of Li from B (Barnes et al. 2019; Romer and Meixner 2014; Straub and Layne 2003; Tomascak et al. 2000). Therefore, it is important to understand the partitioning behavior of Li and B in mineral phases during prograde and retrograde metamorphism in subduction zones, and the role of Li and B exchange between adjacent lithological units, such as between mafic eclogites and meta-sedimentary rocks (Cannaò et al. 2015).

The Changning-Menglian suture zone of SW China is characterized by different eclogites with contrasting pressure–temperature $(P - T)$ paths and peak $P - T$ conditions (Wang et al. 2019, 2020a, 2020b). This region is an outstanding natural laboratory to study the behavior of Li and B in high-P rocks during prograde and retrograde metamorphism. Here we present Li and B concentration data of minerals (omphacite, epidote, amphibole, muscovite, phengite, garnet, chlorite and glaucophane), and Li and B whole-rock isotope data of low-T eclogites, high-T eclogites, and their phengite schist host rocks. We aim to probe into (1) the Li and B behavior in eclogites with different mineral assemblages and contrasting P–T paths; (2) the role of redistribution of Li and B between eclogites and phengite schist wall-rocks during prograde and retrograde processes, (3) the sources and sinks for Li and B during subduction of phengite schists, and (4) the possible cause for variations of Li and B concentrations and isotopic compositions in eclogites.

Geological setting

The Changning–Menglian suture zone is a north–south trending structural zone, bounded by the Kejie-Nandinghe Fault to the west and the Lancangjiang Fault to the east (Fig. 1A; Metcalfe 2021; Ueno et al. 2003). It separates the Baoshan Block (Sibumasu Block) and the Simao Block (a northern fragment of the Indochina Block) (Fig. 1B; Wang et al. 2001; Wu et al. 1995; Zheng et al. 2021). Supra-subduction ophiolites, dated at ca. 270–264 Ma, reflect the east-directed (in modern coordinates) subduction of the main Paleo-Tethys ocean in the Permian (Jian et al. 2009). During

the closure of the Paleo-Tethys in the Early Triassic, relics of the accretionary wedge, including oceanic basalts, limestones, tuffs, clastic rocks, and cherts were thrust onto the eastern flank of the Shan-Thai Block (Zheng et al. 2021). Geochronological and geochemical data suggest that the Lincang granitoids (Fig. 1B) formed during three magmatic episodes, including magmatism related to subduction of the Paleo-Tethys (prior to ~252 Ma), syn-collisional (250–237 Ma), and post-collisional magmatism (235–203 Ma) (Deng et al. 2018).

High-P metamorphic units (Lancang Group), belonging to the accretionary wedge, extend over 400 km along the western flank of the Triassic Lincang granite batholith (Fig. 1B). The Lancang Group mainly consists of metasedimentary rocks with minor intercalations of metamorphic basalt and andesite, and show a tectonic contact to the sedimentary rocks of the Lower Carboniferous Nanduan Formation (Nie et al. 2015). The Nanduan Formation was deposited at the continental margin of the Baoshan Block (Zheng et al. 2019). Garnet–phengite schists and chloritoid–paragonite–phengite schists from the Lancang Group record high-P metamorphism with peak P–T conditions of 1.8–2.4 GPa at 400–650 °C (Wang et al. 2020a). Different types of eclogites and blueschists form lenses and blocks within phengite schists of the Lancang Group (Fan et al. 2015; Wang et al. 2020b). Previous data have shown that these eclogites have E-MORB or N-MORB-like trace element patterns and, therefore, it was suggested that mafic igneous precursors of the eclogites were generated in a mid-ocean-ridge tectonic setting (Wang et al. 2020b). Low-T eclogites include glaucophane eclogites and lawsonite-epidote eclogites, whose peak P–T conditions are estimated to be 2.3–2.6 GPa at 520–610 °C (Fig. 2, Wang et al. 2019, 2020b). In contrast, the peak metamorphic conditions of high-T kyanite eclogites are 2.9–3.2 GPa at 670–750 °C (Fig. 2, Wang et al. 2020b). The high-P mafic and sedimentary rocks reached different depths during subduction and were mechanically juxtaposed during exhumation in the subduction channel (Wang et al. 2020b). Metamorphic zircon U–Pb and phengite $^{40}Ar/^{39}Ar$ isotopic analyses from the phengite schists yield peak metamorphic ages of 238–230 Ma (Wang et al. 2020a). U–Pb dating of metamorphic zircon from low-T and high-T eclogites yields a consistent metamorphic age of ca. 230 Ma (Wang et al. 2020b), similar to the metamorphic zircon ages obtained for the phengite schists.

Sample description

Three types of HP/UHP rocks were investigated: (i) phengite schists, (ii) low-T eclogites, and (iii) high-T eclogites. Sample locations, mineral assemblages, and P–T conditions are presented in Table 1.

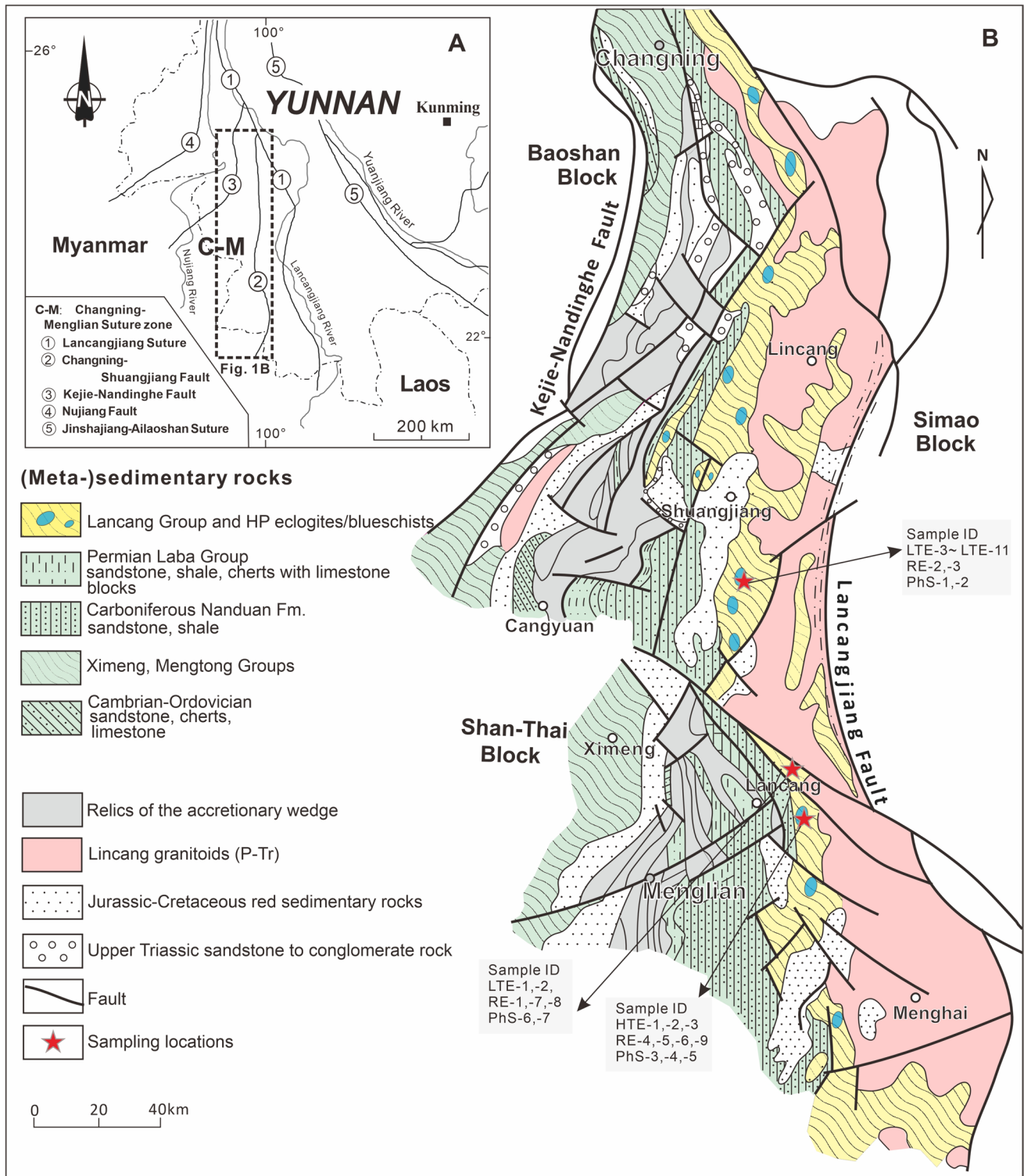**Fig. 1 A** Tectonic subdivision of West Yunnan, highlighting the Changning–Menglian Belt (after Ueno et al. 2003) **B** Geological map of the Changning–Menglian suture zone that separates the Baoshan-Shan Thai Block and the Simao Block (modified after Jin et al. 2003). The sedimentary rocks of the passive margin of the Baoshan Block are in contact with relics of an accretionary wedge (grey unit). The low-T and high-T eclogites and blueschists (blue ellipses) form lenses, blocks and interlayers within the phengite schists of the Lancang Group (yellow unit). Red stars mark sample locations. Detailed sampling coordinates are shown in Table 1

Fig. 2 Metamorphic *P–T* paths for the low-*T* and high-*T* eclogites and garnet phengite schists in the Changning-Menglian suture zone (modified after Wang et al. 2020b). *P–T* paths are defined by mineral compositions and phase assemblage (full lines). Segments of the *P–T* paths not constrained by preserved mineral assemblages are shown as dotted lines. Stability fields of prograde hydrous minerals in mafic rocks and the fields for greenschist facies (GS), blueschist facies (BS), eclogite facies (EC), and amphibolite facies (AM) metamorphism are taken from Wei and Duan (2019). Mineral abbreviations: *Amp* amphibole, *Cld* chloritoid, *Chl* chlorite, *Ep* epidote, *Grt* garnet, *Gln* glaucophane, *Kfs* K-feldspar, *Ky* kyanite, *Lws* lawsonite, *Ms* muscovite, *Omp* omphacite, *Pg* paragonite, *Ph* phengite, *Pl* plagioclase, *Qz* quartz; *Rt* rutile (abbreviations are from Whitney and Evans 2010)
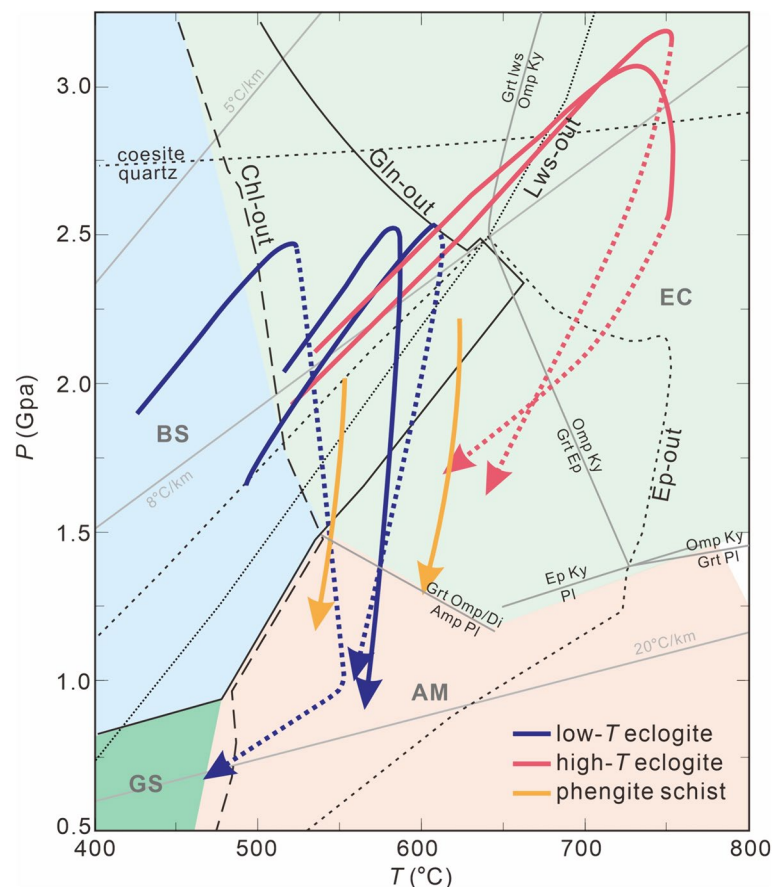
Phengite schist

The typical mineral assemblage of the phengite schist samples includes phengite, garnet, quartz, plagioclase, paragonite, and chlorite (Fig. 3A). Garnet porphyroblasts associated with phengite may reach 0.5–4.0 mm in diameter. The foliation of the matrix is defined by phengite, paragonite, chlorite, biotite, and minor plagioclase (Fig. 3B). Phengite crystals are partially replaced by biotite, paragonite and albite. Phengite has Si contents ranging from 3.1 to 3.6 atoms per formula unit (a.p.f.u.) with low X_{Na} ratios of 0.03 to 0.26. In contrast, paragonite display high X_{Na} ratios of 0.7 to 0.9 and relatively low Si contents of 3.0 to 3.1 a.p.f.u. (Wang et al. 2020a). Chlorite rims around garnet represent a product of late-stage decompression (Fig. 3C).

Low-*T* eclogites

There are three types of low-*T* eclogites, i.e. (i) glaucophane (Gln) eclogite, (ii) lawsonite-epidote (Lws-Ep) eclogite, and (iii) partially retrogressed (amphibolitized) eclogite. Glaucophane eclogite consists mainly of garnet, omphacite, glaucophane, phengite, epidote, rutile, chlorite, and quartz (Fig. 3D). Garnet in Gln eclogite has 1 to 2 mm

diameter. Garnet porphyroblasts have compositions of $Prp_{8–18}Alm_{63–69}Grs_{16–22}Sps_{1–6}$ and contain inclusions of quartz, epidote, glaucophane, omphacite, augite, and rutile. Omphacite in the matrix has Di (Ca/Ca + Na) and Jd (Al_{VI}/(Na + Ca)) values ranging from 0.42 to 0.48 and 0.39 to 0.55, respectively (Wang et al. 2020b). Phengite occurs irregularly in the matrix (Fig. 3D). It has high Si values of 3.4 to 3.6 a.p.f.u (Wang et al. 2020b). Lws-Ep eclogite contains garnet, omphacite, epidote, lawsonite, glaucophane, phengite, rutile, chlorite, and quartz (Fig. 3E). The name-giving feature is the presence of lawsonite, which coexists with epidote in the matrix. Lawsonite is partially to completely replaced by late epidote (Wang et al. 2020b). Minor amounts of lawsonite also occur as inclusions in garnet (Wang et al. 2020b). Chlorite is a secondary phase that formed during garnet decomposition (Fig. 3D,E).

Retrogressed, partially amphibolitized eclogite has variable proportions of secondary mineral phases, including amphibole, chlorite, and plagioclase. Omphacite was partially replaced by amphibole and plagioclase in the retrogressed samples, leaving garnet as porphyroblasts with coatings of chlorite. Phengite is heterogeneously distributed in the rock. It forms local aggregations and is commonly concentrated in deformation tails of garnet.

Table 1 Sample locations, mineral assemblages, and *P*–*T* conditions for low-*T* and high-*T* eclogites, amphibolitized eclogite, and phengite schists from the Changning-Menglian suture zone

Sample ID		Rock name	Longitude	Latitude	Mineral assemblage	*P* GPa	*T* °C
High-*T* eclogites							
18J75-1.1	HTE-1	Grt-Omp eclogite	100° 08′ 14.25″	22° 32′ 56.49″	Omp+Grt+Aug+Ep+Amp+Pl+Qz+Chl+Ms		
18J75-11.4	HTE-2	Ky eclogite	100° 08′ 16.35″	22° 32′ 56.10″	Omp+Grt+Amp+Ky+Ep±Pg+Qz+Chl+Ms	2.9–3.1	700–750
18J75-14.5	HTE-3	Grt-Omp eclogite	100° 08′ 14.25″	22° 32′ 56.49″	Omp+Grt+Aug+Ep+Amp+Pl+Qz+Chl+Ms		
Low-*T* eclogites							
18J74-1.9	LTE-1	Gln eclogite	100° 04′ 25.13″	22° 37′ 26.23″	Omp+Grt+Ph+Qz±Ep+Chl		
18J74-1.10	LTE-2	Gln eclogite	100° 04′ 25.13″	22° 37′ 26.23″	Omp+Grt+Gln+Ms+Ep+Qz+Chl	2.3–2.6	580–610
18J77-13.1d	LTE-3	Lws-Ep eclogite	99° 49′ 00.77″	23° 13′ 23.70″	Omp+Grt+Ms+Ep+Qz+Lws+Chl		
18J77-16	LTE-4	Lws-Ep eclogite	99° 49′ 00.77″	23° 13′ 23.70″	Omp+Grt+Ep+Ms+Qz+Lws+Chl	2.4–2.6	520–530
18J77-10.7	LTE-5	Lws-Ep eclogite	99° 49′ 00.77″	23° 13′ 23.70″	Omp+Grt+Gln+Pg+Ms+Ep+Qz+Lws+Chl		
18J77-8.7	LTE-6	Gln eclogite	99° 49′ 00.77″	23° 13′ 23.70″	Omp+Grt+Gln+Ms+Ep+Qz±Lws+Chl		
18J77-8.4	LTE-7	Gln eclogite	99° 49′ 00.77″	23° 13′ 23.70″	Omp+Grt+Gln+Ms+Ep+Qz±Lws+Chl		
18J77-1.2	LTE-8	Lws-Ep eclogite	99° 49′ 00.77″	23° 13′ 23.70″	Omp+Grt+Ep+Qz+Lws+Chl		
18J77-2.3	LTE-9	Lws-Ep eclogite	99° 49′ 00.77″	23° 13′ 23.70″	Omp+Grt+Ep+Ph+Qz+Lws+Chl		
18J77-7.4	LTE-10	Lws-Ep eclogite	99° 49′ 00.77″	23° 13′ 23.70″	Omp+Grt+Ep+Ph+Qz+Lws+Chl		
18J77-7.8	LTE-11	Lws-Ep eclogite	99° 49′ 00.77″	23° 13′ 23.70″	Omp+Grt+Ep+Ph+Qz+Lws+Chl		
Retrograde eclogites							
18J74-1.7	RE-1	Amphibolitized eclogite	100° 04′ 25.13″	22° 37′ 26.23″	Grt+Omp+Amp+Ep±Pl		
18J77-14	RE-2	Amphibolitized eclogite	99° 49′ 00.77″	23° 13′ 23.70″	Amp+Pl+Chl±Grt		
18J78-20	RE-3	Amphibolitized eclogite	99° 49′ 52.08″	23° 13′ 18.57″	Amp+Pl+Ep+Ph		
18J75-14.1a	RE-4	Amphibolitized eclogite	100° 08′ 14.25″	22° 32′ 56.49″	Amp+Pl+Grt		
18J75-14.2	RE-5	Amphibolitized eclogite	100° 08′ 14.25″	22° 32′ 56.49″	Amp+Pl+Grt+Chl		
18J75-14.3	RE-6	Amphibolitized eclogite	100° 08′ 14.25″	22° 32′ 56.49″	Amp+Pl+Grt+Chl		
18J74-1.1	RE-7	Amphibolitized eclogite	100° 04′ 25.13″	22° 37′ 26.23″	Grt+Omp+Amp+Pl		
18J74-1.11	RE-8	Amphibolitized eclogite	100° 04′ 25.13″	22° 37′ 26.23″	Grt+Omp+Ep+Pl+Amp+Ph		
18J76-1.4	RE-9	Amphibolitized eclogite	100° 07′ 00.94″	22° 31′ 34.37″	Amp+Pl+Qz±Grt		
Phengite schists							
18J88-1.3	PhS-1	Garnet phengite schist	99° 50′ 08.57″	23° 13′ 46.01″	Grt+Pl+Qz+Ph+Chl	1.9–2.4	400–650
18J82-3.3	PhS-2	Garnet phengite schist	99° 50′ 10.31″	23° 16′ 15.59″	Grt+Pl+Qz+Ph+Chl		
18J75-14.1b	PhS-3	Phengite schist	100° 08′ 14.25″	22° 32′ 56.49″	Ph+Pl+Qz+Chl		
18J75-15.1	PhS-4	Phengite schist	100° 08′ 14.25″	22° 32′ 56.49″	Ph+Pl+Qz+Chl		
18J75-16.1	PhS-5	Garnet phengite e schist	100° 08′ 14.25″	22° 32′ 56.49″	Grt+Ph+Pl+Qz+Chl		
18J74-2	PhS-6	Phengite schist	100° 04′ 25.13″	22° 37′ 26.23″	Ph+Pl+Qz+Chl		
18J74-3	PhS-7	Garnet phengite schist	100° 04′ 25.13″	22° 37′ 26.23″	Grt+Ph+Pl+Qz+Chl		

Sample names starting with 18J are field names and have been used in earlier publications. HTE-x, LTE-x, RE-x, and PhS-x are the names used here, consisting of an abbreviation of the rock type and a running number (x)

Amp amphibole, *Aug* augite, *Chl* chlorite, *Ep* epidote, *Gln* glaucophane, *Grt* garnet, *Ky* kyanite, *Lws* lawsonite, *Omp* omphacite, *Pl* plagioclase, *Ph* phengite, *Pg* paragonite, *Qz* quartz, *Ms* muscovite

The *P*–*T* data source from Wang et al. (2019; 2020a; 2020b)

High-*T* eclogites

There are two types of high-*T* eclogites: garnet-omphacite (Grt-Omp) eclogite and kyanite (Ky) eclogite. Grt-Omp eclogite has a simple peak metamorphic mineral assemblage consisting of omphacite and garnet. Garnet porphyroblasts have compositions of $Prp_{14-28}Alm_{62-71}Grs_{10-14}Sps_{1-3}$. Omphacite shows Di and Jd values ranging from 0.4 to 0.5
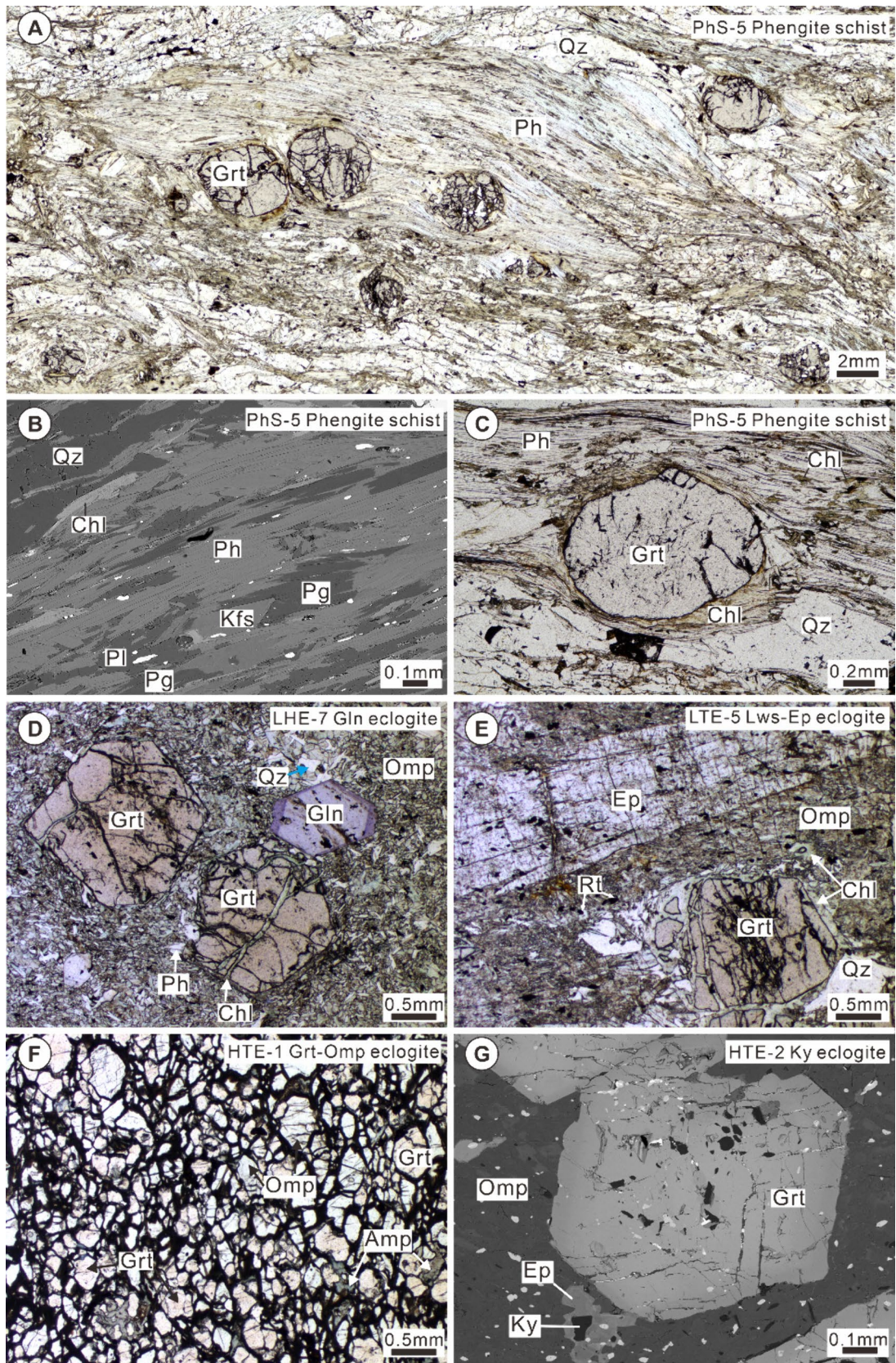
◀**Fig. 3** Photomicrographs of phengite schist, low-T eclogites and high-T eclogites in the Changning-Menglian suture zone. **A–C** Phengite is partially replaced by biotite, paragonite and albite. Chlorite forms retrograde rims around garnet. **D–E** The peak mineral assemblage of the low-T eclogites is mainly $Grt + Omp + Gln + Lws + Ph \pm Ep$. Chlorite is a secondary phase formed at the expense of garnet upon retrogression. **F–G** The peak mineral assemblage of the high-T eclogites is $Grt + Omp + Ky + Ph/Pg \pm Ep$. Garnet and omphacite were partially replaced by albite, Ca-amphibole, and augite during retrogression. Detailed mineral assemblages are listed in Table 1. Mineral abbreviations are the same as in Fig. 2

and 0.49 to 0.61, respectively. Retrogression of Grt-Omp eclogite under greenschist facies conditions led to the partial replacement of garnet and omphacite by an assemblage of epidote, albite ($An_{22-42}Ab_{58-78}$), Ca-amphibole ($Ca_B = 1.53–1.69$ a.p.f.u., $X_{Mg} = 0.59–0.64$), and augite ($Di_{87-90}Jd_{10-13}$) (Fig. 3F, Wang et al. 2021). In addition, there is accessory muscovite, rutile, clinozoisite, and opaque oxides.

Kyanite eclogite comprises omphacite, garnet, rutile, kyanite, epidote, phengite, quartz, dolomite, and magnesite (Fig. 3G). The composition of garnet porphyroblasts is $Prp_{10-32}Alm_{46-68}Grs_{17-24}Sps_{<5}$. Omphacite has similar compositions as omphacite in Grt-Omp eclogite, showing Di and Jd values of 0.4–0.5 and 0.42–0.59, respectively (Wang et al. 2020b). Kyanite occurs in the rims of garnet and as intergrowths with epidote in the matrix (Fig. 3G).

Analytical methods

Whole-rock major and trace elements

Whole rock (WR) major and trace element concentrations were determined at the Wuhan Sample Solution Analytical Technology Co., Ltd., Wuhan, China. Major element compositions were analyzed on fused glass discs using a Zsx Primus II wavelength dispersive X-ray fluorescence spectrometer (XRF) produced by RIGAKU, Japan. Samples were dried at 105 °C before determining loss on ignition (LOI) and producing fused glass disks. Samples were melted in Pt crucibles at 1050 °C using a mixture of lithium tetraborate, lithium metaborate, and lithium fluoride (45:10:5) as flux. Ammonium nitrate and lithium bromide were used as oxidant and release agent respectively. The major element results for the reference materials GBW07103, GBW07105, GBW07111, and GBW07112 are shown in Table S1. The relative standard deviation (RSD) is less than 2% for the analyzed elements.

Trace element compositions were analyzed by inductively coupled plasma mass spectrometry (ICP–MS) using an Agilent 7700e system. Sample powders (~ 50 mg) were digested in a mixture of suprapure 14 mol/L HNO_3 and 22 mol/L HF in Teflon-lined stainless-steel autoclaves at 190 ℃, evaporated to near dryness. The samples were re-dissolved by adding 1 mL HNO_3 (14 mol/L), 1 mL MQ H_2O and 1 mL internal standard In (1 ppm), and resealed and heated in the autoclaves at 190 ℃ for over 12 h. The final solutions were diluted to 100 g with a mixture of 2% HNO_3 for ICP-MS analysis. Indium was used as an internal standard to correct for matrix effects and instrument drift. The reference materials AGV-2, BCR-2, and RGM-2 were analyzed to monitor the data quality (Table S1). The analytical precision and accuracy were estimated better than $\pm 10\%$ RSD (relative standard deviation) for most trace elements.

Mineral trace elements

In situ trace element analysis was conducted at the Institute of Geology, Chinese Academy of Geological Sciences, Beijing. The NWR 193[UC] laser ablation system (Elemental Scientific Lasers, USA) was equipped with a Coherent Excistar 200 excimer laser and a two-volume ablation cell. The ablation system was coupled to an Agilent 7900a ICP-MS (Agilent, USA). Pre-ablation was conducted for each spot analysis using five laser shots to remove potential surface contamination. This study used a 50 μm spot diameter, a 10 Hz repetition rate, and a fluence of 4 J/cm². The Iolite software package was used for data reduction (Paton et al. 2011). NIST 610 and BCR-2G were used as primary and secondary reference materials, respectively. Analytical precision for most elements in BCR-2G vary from 1 to 5% RSD, based on the repeated analysis of unknown samples and certified reference materials (Jochum et al. 2005). Triplets of reference material bracketed each group of 8–10 analyses of unknown samples. Typically, 35–40 s of the sample signals were acquired after 20 s of background measurement. ^{43}Ca was used as an internal standard to calibrate trace element concentrations for amphibole and clinopyroxene. ^{29}Si was adopted as internal standard for chlorite, micas, and garnet. SiO_2 and CaO contents of the above silicate minerals were determined by electron microprobe.

Li and B isotopes

Lithium and boron concentrations and isotopic compositions of the whole-rock samples of eclogites and phengite schists were analyzed using a Thermo Element NEPTUNE MC-ICPMS instrument at GFZ German Research Centre for Geosciences, Potsdam (Germany). For Li isotope analysis, samples were dissolved in HF on the hotplate. Lithium was separated from the matrix using a two-step ion exchange procedure using Biorad AG50W resin. The second step removes Na remaining after the first separation.
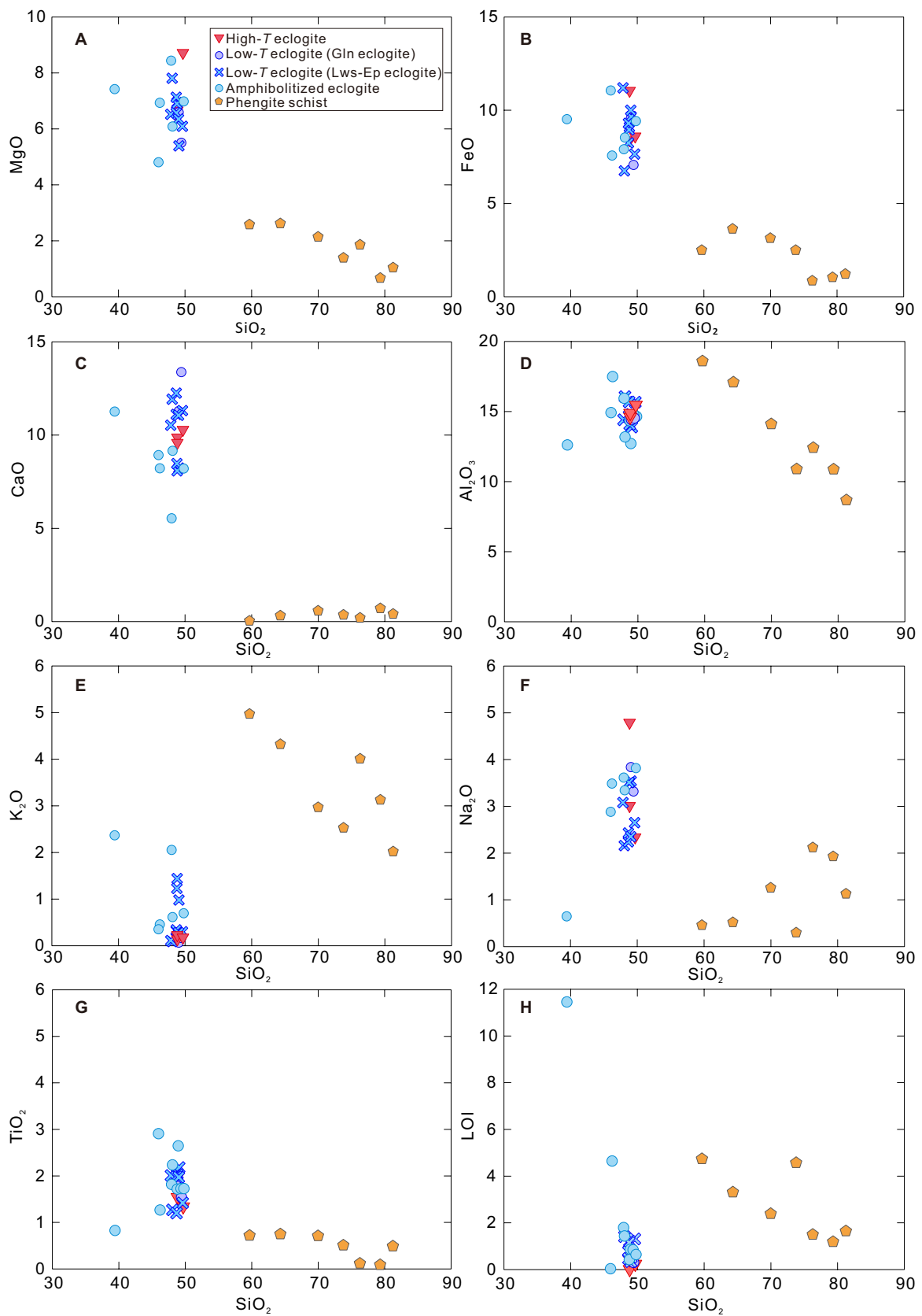
◄**Fig. 4** SiO_2 vs selected major elements [wt.%]. **A** SiO_2 vs. MgO. **B** SiO_2 vs. FeO. **C** SiO_2 vs. CaO. **D** SiO_2 vs. Al_2O_3. **E** SiO_2 vs. K_2O. **F** SiO_2 vs. Na_2O. **G** SiO_2 vs. Ti_2O. **H** SiO_2 vs. LOI (Loss of ignition). The binary trend for the schists indicates the effect of the dilution of their protolith by quartz. The eclogites show basaltic compositions similar to the oceanic crust (Klein 2003). The retrograde amphibolitized eclogites have increased K_2O, LOI (H_2O), and decreased CaO, indicating that exhumation took place in an open system facilitating element transport

As Li loss during ion-exchange separation causes isotopic fractionation (Tomascak et al. 1999), we collected and analyzed pre-Li eluate and post-Li eluate fractions for all samples to assure by mass balance that procedural loss of Li was less than 0.1% of the total Li in the samples. For quality control, we analyzed rock powder reference materials (JG2 and JR2) with each set of 10 unknown samples (Romer et al. 2014; Xu et al. 2021). For B isotope analysis, the samples were decomposed by alkaline fusion at 950 °C for 90 min using K_2CO_3 as flux. After cooling, boron was leached quantitatively from the melt cake at ~ 80 °C and the supernatant solution was separated from the insoluble material. Boron was collected from this solution by adding B-specific resin Amberlite IRA743 and keeping the sample at 60 °C for 2 days. Thereafter, boron was separated from the matrix using a two-step ion exchange procedure, using Amberlite IRA743 and Biorad AG50W resins, respectively. Each sample series included two reference materials and a procedural blank (Romer et al. 2014; Xu et al. 2021).

Data collection for Li and B isotopic compositions was performed in the standard-sample-standard bracketing mode. Samples and reference materials were diluted in 2% HNO_3 to approximately 25 ppb Li and 50 ppb B in solution, respectively, to avoid bias from potentially contrasting Li and B concentrations. Before and after each sample and each reference material, the background intensity of 2% HNO_3 was determined. The average of these two background values was used as an instrumental baseline to correct signal intensities of the bracketed sample or reference material. For B analysis, memory effects in the sample introduction system were suppressed by using an additional wash step using 2% HNO_3 containing dilute HF after each sample or reference material. Lithium and B isotopic compositions are reported as δ^7Li ($\delta^7Li = \{[(^7Li/^6Li)_{sample}/(^7Li/^6Li)_{reference\ material}]-1\} \times 1000$) and $\delta^{11}B$ ($\delta^{11}B = \{[(^{11}B/^{10}B)_{sample}/(^{11}B/^{10}B)_{reference\ material}]-1\} \times 1000$), respectively, relative to the reference materials NIST SRM 8545 (for Li) (Flesch et al. 1973) and NBS SRM 951 (for B) (Catanzaro et al. 1970). Each sample solution was typically measured six times in two independent analytical sessions. Each sample series included two geological reference materials that were treated as unknowns and were used to monitor the accuracy of the analytical methods and instrumental routines. The average δ^7Li of the two reference materials

JG2 and JR2 (cf. Romer et al. 2014) determined during the same measurement period are $+0.13 \pm 0.04$ ‰ (2σ, n = 14) and $+4.01 \pm 0.07$ ‰ (2σ, n = 15), respectively. The average $\delta^{11}B$ of the two B reference materials TB and TS (Govindaraju 1994; Romer et al. 2014) determined during the same measurement period are $+11.31 \pm 0.09$ ‰ (2σ, n = 13) and $+13.94 \pm 0.11$ ‰ (2σ, n = 14), respectively. These values are consistent with literature data published for these reference materials (Jochum et al. 2005, GeoReM database, http://georem.mpch-mainz.gwdg.de/). The concentrations of Li and B of the samples were determined by comparing the signal intensities of ^{11}B and ^7Li, respectively, of adequately diluted, chemically purified sample solutions on the NEPTUNE MC-ICPMS instrument with those obtained from a calibrated 50 ng g^{-1} B reference solution of NBS SRM 951 (for B) and from a 25 ng g^{-1} Li reference solution of NIST SRM 8545 (for Li). Calculated mass fractions of B and Li for the reference materials JG2, JR2 (for Li) and TB, TS (for B) collected over a period of several years generally agree with published reference values, and are reproducible within a range of $\pm 10\%$ (1σ) for both B and Li.

In-situ element mapping by LA-ICP-MS

LA-ICP-MS in situ imaging was conducted by LA-ICP-MS at the Wuhan SampleSolution Analytical Technology Co., Ltd., Wuhan, China using a NEW193HE laser and an Agilent 8900 ICP-MS Triple Qua instrument. Helium was applied as a carrier gas. Argon was used as make-up gas and mixed with the carrier gas via a T-connector before entering the ICP. The spot size and frequency of the laser were set to 10×10 μm and 10 Hz with a movement rate of 6 μm/s. The trace elements were calibrated against NIST 610 glass as an external calibration (Liu et al. 2008). The map is semi-quantitative as we did not use internal standardization during analyses. Off-line selection and integration of background and analyzed signals, time-drift correction, and quantitative calibration for trace element analysis used the Iolite software (Paton et al. 2011). The XMapTools software was used to optimize the element maps (Lanari et al. 2014, 2019).

Results

Whole-rock major and trace elements

The phengite schists have high SiO_2 (59.7–81.3 wt.%) and K_2O (2.02–4.97 wt.%) and low MgO (0.67–2.62 wt.%), FeOt (t-total Fe calculated as FeO) (1.26–6.97 wt.%), CaO (0.04–0.71 wt.%), Na_2O (0.30–2.12 wt.%), and TiO_2 (0.09–0.75 wt.%) contents (Fig. 4 and Table S1). Furthermore, the phengite schists are characterized by LREE enrichments and HREE depletions with high $La_N/$

Yb_N ratios of 3.7–17.2. They display pronounced negative Eu anomalies (Eu/Eu* $((Eu_N/(Sm_N \times Gd_N)^{1/2}) = 0.4$–0.8) (Fig. S1). Trace element diagrams normalized to primitive mantle composition show that the samples are enriched in LILE elements (e.g. Cs, Rb, K, and Pb) and have negative anomalies for Nb, Ta, and Sr (Fig. S1).

Low-T and high-T eclogite samples have similar major and trace element compositions, except for sample RE-3 which is enriched in muscovite and carbonate minerals and shows extremely low SiO_2 contents (39.5 wt.%) and high LOI (11.4 wt.%) (Fig. 4). The other samples show consistent SiO_2 (46.0–49.9 wt.%), Al_2O_3 (12.7–17.5 wt.%), Na_2O (2.2–4.8 wt.%), and TiO_2 (1.2–2.9 wt.%) contents (Fig. 4). Their FeOt (10.8–18.7 wt.%), CaO (5.63–13.4 wt.%), MgO (4.9–8.7 wt.%), and K_2O (0.1–2.1 wt.%) are variable (Fig. 4). Mg# values are between 43 and 65. The Cr and Ni contents in the eclogites range from 52.1–467 ppm and 28.4–137 ppm, respectively (Table S1).

In chondrite-normalized trace element diagrams, the low-T, high-T and amphibolitized eclogites have fractionated rare earth element (REE) patterns with La_N/Yb_N ratios of 1.3–4.5 (Fig. S1). Most samples are enriched in LILE (Cs, Rb, K, and Pb), and have negative Ba, and Sr anomalies (Fig. S1). Some samples show negative Pb anomalies (Fig. S1), as well as negative K anomalies.

Li and B contents in minerals

Lithium and B contents in minerals from the phengite schists, low-T eclogites, and high-T eclogites are presented in Table S2. Mineral inclusions such as kyanite and lawsonite were not analyzed due to their tiny grain sizes.

Phengite schist (PhS-5 and PhS-7)

Phengite crystals from two phengite schists exhibit similar Li contents ranging from 7.4 to 32.9 ppm, but they show contrasting B contents, with 88–128 ppm in sample PhS-7 and 37.9–61.7 ppm in sample PhS-5 (Table S2 and Fig. 5A,B). Within individual phengite grains, there are negligible variations in Li and B from the core to the rim (Fig. S2). Paragonite has Li concentrations of 6.6–9.4 ppm and high B concentrations of 184–234 ppm. In contrast, chlorite is fairly rich in Li (38.6–78.1 ppm) but has low B contents (4.8–13.5 ppm). Garnet crystals have Li contents between 0.5 and 16.0 ppm (Table S2). Garnet, quartz, and plagioclase crystals have B contents below the detection limit (< 0.3 ppm). The Li and B distribution among the metamorphic minerals demonstrates that the Li and B budget of the whole rock samples is dominated by phengite and chlorite (Fig. 5A and B).

Low-T eclogite

Gln eclogite (LTE-7)

Omphacite has high concentrations of Li (9.1–28.6 ppm) and only minor concentrations of B (0.9–2.6 ppm) (Fig. 5C). The Li contents of glaucophane are comparable to those of omphacite, between 4.6 and 35.6 ppm, whereas the B contents are slightly higher than in omphacite, varying from 0.9 to 4.3 ppm (Fig. 5C). Chlorite has higher Li contents than omphacite, ranging from 34.1 to 52.5 ppm. The B concentrations in chlorite are between 1.0–3.2 ppm. Garnet has low abundances of Li (0.5–5.0 ppm) and B (< 0.6 ppm), whereas phengite has high and variable concentrations of Li (3.7–31.2 ppm, av. 12.7 ppm) and B (18.2–68.0 ppm, av. 30.9 ppm).

Lws-Ep eclogite (LTE-5)

The Li and B contents of omphacite in sample LTE-5 range from 13.7–18.4 ppm and 0.4–1.9 ppm, respectively (Fig. 5D). Chlorite has high Li and B concentrations of 38.8–49.0 ppm and 2.5–6.1 ppm, respectively. Epidote and garnet have low Li contents of 0.1–2.1 ppm (epidote) and 0.7–3.3 ppm (garnet), and B contents near or below the detection limit (Fig. 5D). Lawsonite occurs only as inclusions in garnet that is too tiny to be analyzed.

High-T eclogite (HTE-1 and HTE-2)

Grt-Omp eclogite (HTE-1)

Among the prograde metamorphic minerals, omphacite has high Li (10.6–105 ppm) and low B (0.8–1.7 ppm) abundances (Fig. 5E), whereas garnet shows low Li contents (mostly < 0.5 ppm) and B contents (typically below the detection limit) (Table S2). Among the retrograde minerals, amphibole contains 2.6–10.8 ppm Li and 6.2–16.1 ppm B, while muscovite hosts 25.6–31.1 ppm Li and 22.3–47.3 ppm B (Fig. 5E).

Ky eclogite (HTE-2)

Omphacite has Li and B contents varying from 22.6–42.3 ppm and 0.3–1.5 ppm, respectively (Fig. 5F). Epidote and garnet have low B contents (mostly below the detection limit). Epidote has lower Li concentrations (0.7–19.0 ppm) than omphacite, but higher Li contents than garnet (0.4–3.6 ppm; Fig. 5F). Amphibole has variable Li (5.5–52.5 ppm, av. 25.5 ppm) and B (5.5–20.5 ppm, av. 13.2 ppm) concentrations. Retrograde muscovite contains high contents of both Li (37.4–297 ppm, av. 93.5 ppm) and B (131–430 ppm, av. 305 ppm).
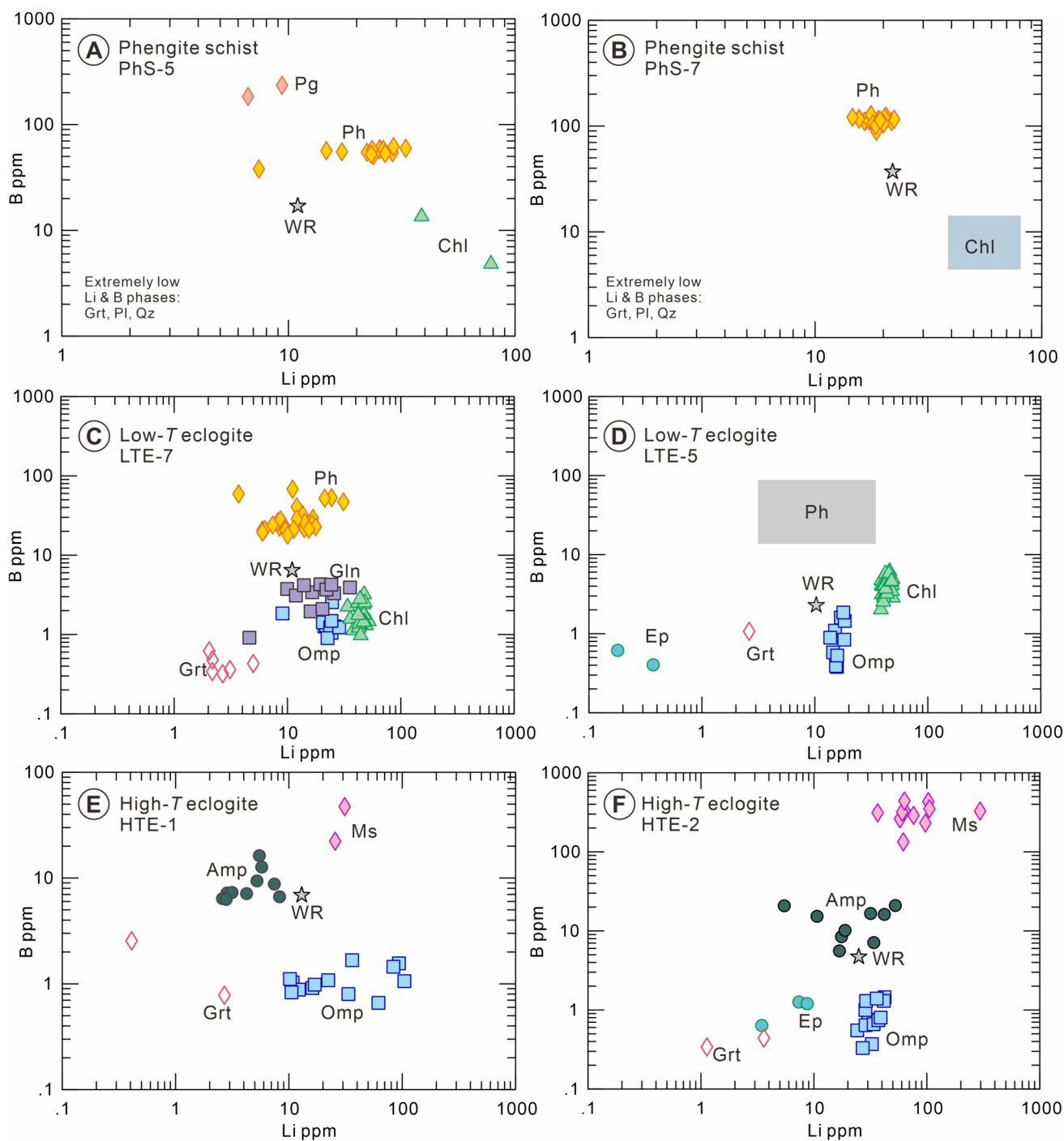
Fig. 5 Li and B contents in minerals from **A,B** phengite schists, **C,D** low-*T* eclogites and **E,F** high-*T* eclogites from the Changning-Menglian suture zone (Data from Table S2). Phengite is the dominant host of Li and B in schists samples. Omphacite controls the Li budget of low-*T* and high-*T* eclogites. Phengite, amphibole, and muscovite dominate the B budget of the whole-rock eclogite samples. Chlorite in panel 5D is retrograde and also contributes to the B budget of this sample. Furthermore, phengite (not observed in the analyzed thin section) occurs irregularly in the sample for this location. Even minor contributions of phengite dominate the B budget of the whole rock sample. The mass balance of Li and B for different minerals is shown in Table 2. Abbreviations are the same as in Fig. 2
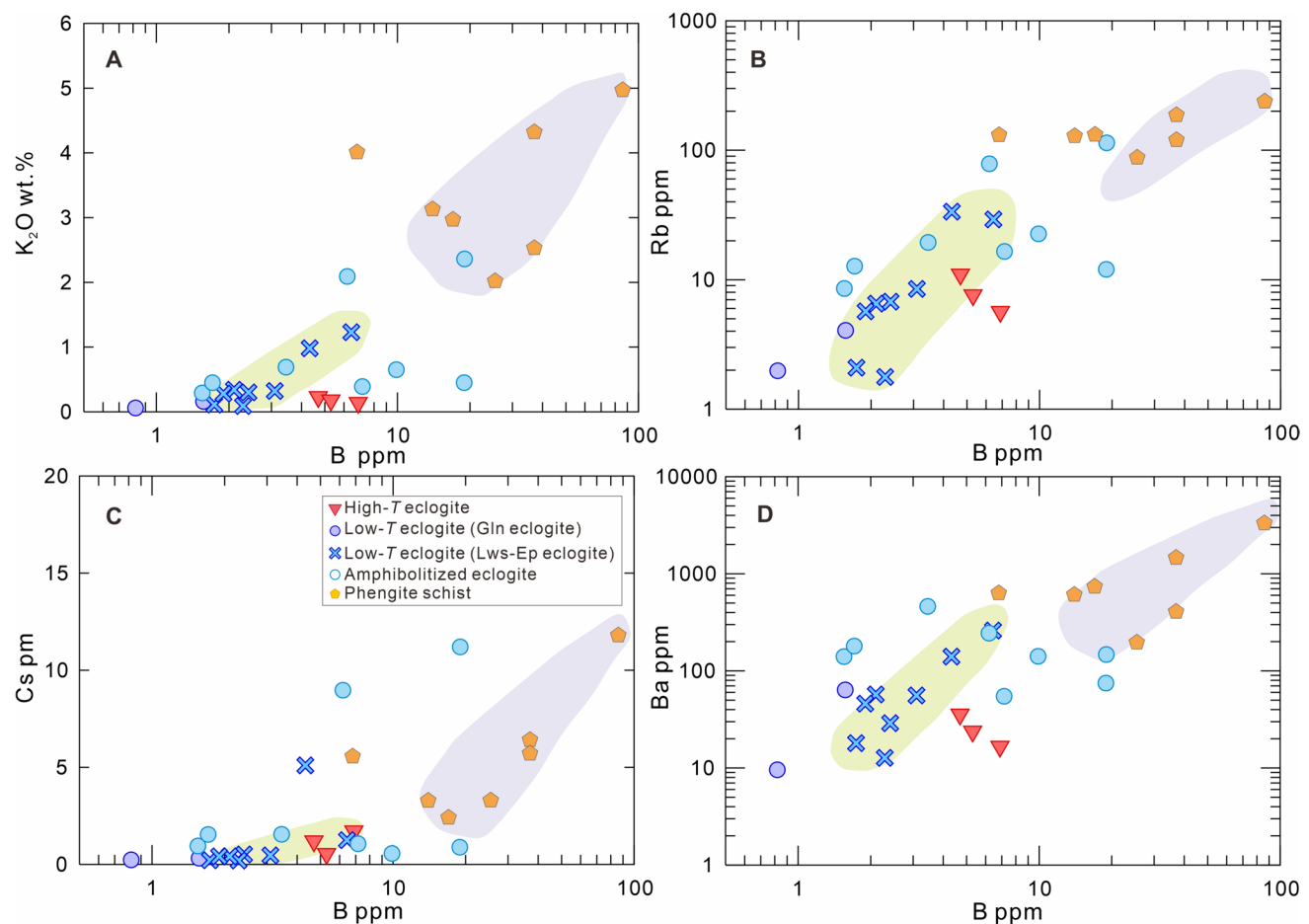
Fig. 6 The whole-rock B contents vs. selected major and trace elements for low-*T* and high-*T* eclogites, amphibolitized eclogites, and phengite schists from the Changning-Menglian suture zone. **A** K₂O [wt.%] vs. B [ppm]. **B** Rb [ppm] vs B [ppm]. **C** Cs [ppm] vs B [ppm]. **D** Ba [ppm] vs B [ppm]. The B contents increase with increasing K₂O, Rb, Cs, and Ba contents. The variation of B along with these mobile elements reflects that the B budget in the phengite schists and low-*T* eclogites is mainly controlled by phengite

Whole-rock Li and B contents and isotope data

Lithium and B contents and isotopic compositions of the whole-rock samples are shown in Table S1 and Figs. 6 and 7. Low-*T* eclogite and high-*T* eclogite samples have overlapping ranges of Li concentrations ranging from 4.9 to 27.0 ppm, significantly higher than the depleted mantle (1.0 to 1.5 ppm, Li, Seitz and Woodland (2000) (Fig. 7B). The δ^7Li values vary from -5.5 to $+4.3$ ‰ in low-*T* eclogites and amphibolitized eclogites. In contrast, high-*T* eclogites have distinctly lower δ^7Li values of -13.2 to -5.8 ‰ (Fig. 7B). Phengite schists have Li contents and δ^7Li ranging from 8.7 to 27.0 ppm and -3.8 to $+3.0$ ‰, respectively. Their δ^7Li values fall within similar ranges as samples of low-*T* and amphibolitized eclogites (Fig. 7B).

The low-*T* eclogites and high-*T* eclogites have B concentrations varying from 0.8 to 7.9 ppm. Two samples of amphibolitized eclogite have B contents above 10 ppm (Fig. 7C). All eclogite samples have negative δ^{11}B values ranging from

-17.7 to -6.6 ‰ (av. -11.0 ‰). The B contents in the phengite schists are more variable, ranging from 6.8 to 86.0 ppm, and much higher than the B contents of the majority of eclogite samples (Fig. 7C). The δ^{11}B values of phengite schists are also negative, ranging between -22.8 and -9.5 ‰ (av. -13.6 ‰).

In-situ Li and B mapping of the phengite schists

Figure 8 shows in-situ element maps for sample PhS-5 that mainly consists of phengite, paragonite, plagioclase, and chlorite. While the element maps largely reflect the distribution of minerals and the rock texture, the maps also show that some minerals are heterogeneous. For instance, the contents of Si, Al, K and B are heterogeneous within phengite. Toward paragonite, the contents of Si, K, and B in phengite decrease. Boron is heterogeneously distributed in both paragonite and phengite and shows a positive correlation with Sr in paragonite. Paragonite shows much
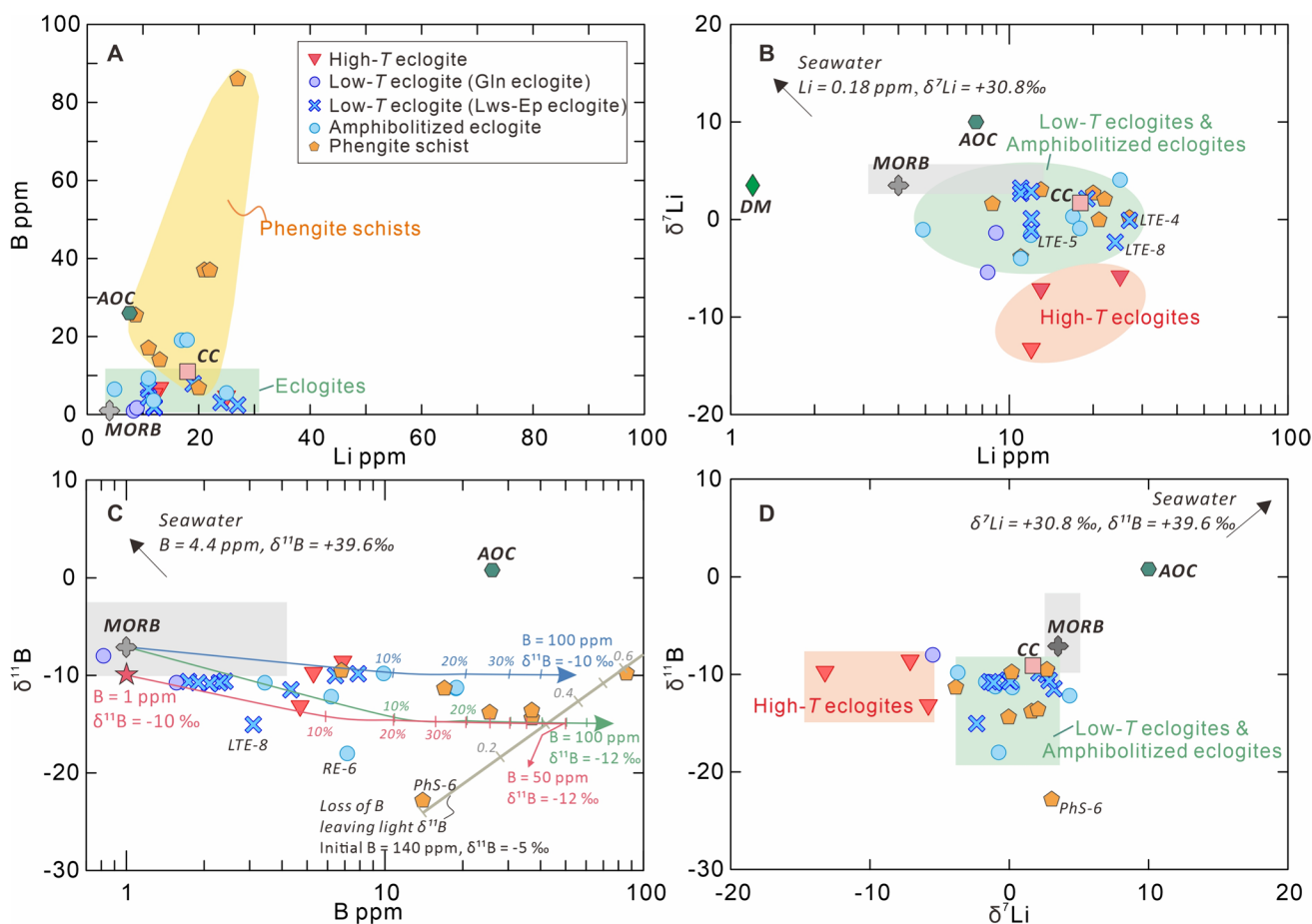
Fig. 7 Variations of the Li and B contents and isotopic compositions (Data from Table S1) of the phengite schists and low-T and high-T eclogites from the Changning-Menglian suture zone. **A** B [ppm] vs. Li [ppm]. Phengite schists have much higher B contents than low-T and high-T eclogites, although their Li contents are similar. **B** Li [ppm] vs. δ^7Li. Low-T and amphibolitized eclogites plot in a similar range as phengite schists. The high-T eclogites show extremely low δ^7Li values. **C** B [ppm] vs. δ^{11}B. B leaching from the phengite schists would induce the loss of B and decrease of δ^{11}B values. Low-T and high-T eclogites have variable B contents with negative δ^{11}B, probably controlled by B metasomatism sourced in the phengite schists. **D** δ^7Li vs. δ^{11}B. The low-T and amphibolitized eclogite fields overlap with the phengite schist signature. Li was added from the phengite schists to the eclogites (see details in the text and Fig. 9). High-T eclogites show very low δ^7Li, indicating that they either have experienced strong loss of water and Li, or have exchanged with wall rocks characterized by low δ^7Li values during prograde metamorphism. *AOC* altered oceanic crust, *CC* continental crust, *DM* depleted mantle, *MORB* mid-ocean ridge basalt. End member values and ranges for Li and B are from Teng et al. (2008) and Marschall et al. (2017)

higher Sr contents than phengite. Paragonite has relatively low Rb concentrations, which is predominantly hosted by phengite. Lithium shows a strong correlation with Mg in both chlorite and phengite, which are the main carriers of Li in sample PhS-5. In contrast, paragonite and plagioclase display very low Li contents.

Discussion

Lithium redistribution and isotopic fractionation during high-pressure metamorphism and exhumation

Li isotopic behavior in subduction zones

The material entering subduction zones and affected by prograde metamorphism typically has a wide range of initial δ^7Li values. For instance, the Li isotopic composition of continental crust and mantle rocks typically falls in the δ^7Li range of 0 to +5.6 ‰ (e.g. Bebout and Penniston-Dorland 2016; Tomascak 2004; Tomascak et al. 2016). Major
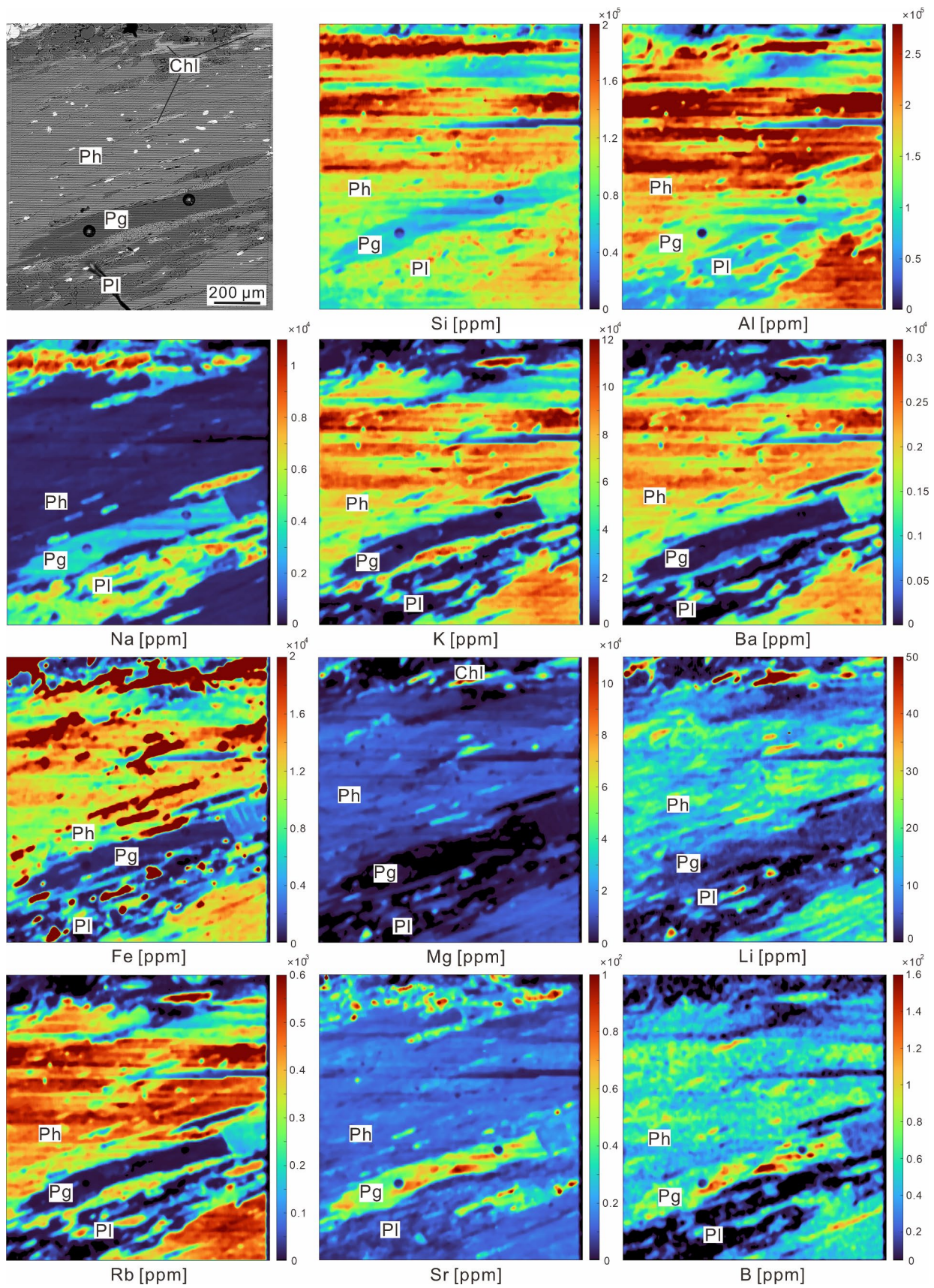
◀**Fig. 8** LA-ICPMS element maps for selected elements of phengite schist PhS-5. The color bar to the right of each panel represents the element concentrations (note the different scales). Lithium is mainly hosted in phengite. Boron is heterogeneously distributed in phengite and paragonite

rock types with δ^7Li values that are not restricted to this narrow range include intensely weathered rocks, marine sediments, altered oceanic crust, high-grade metamorphic rocks, serpentinites, arc volcanic rocks, granites, and related ore deposits (Tomascak et al. 2016). Establishment of the broader range of Li isotopic compositions in different groups of rocks follows the main principal process: fluid–rock interaction results in the redistribution of Li between the rocks (minerals of the rocks) and the fluid, whereby the fluid typically acquires a higher δ^7Li than the solid (Benton et al. 2004; Wunder et al. 2007). The redistribution of Li during intense chemical weathering results in the loss of isotopically heavy Li from the rock, which decreases δ^7Li of the weathered rocks that are commonly rich in clay minerals. Therefore, crustal rocks that experienced intense chemical weathering may have very low δ^7Li values (Rudnick et al. 2004; Romer et al. 2014). Modern seawater has a high δ^7Li value ($+31.0 \pm 0.1$ ‰; Millot et al. 2004; Misra and Froelich 2012), largely due to the formation of authigenic minerals and partitioning of ^7Li into the liquid phase during weathering (e.g. Andrews et al. 2020). The interaction between fluids and MORB will result in variable δ^7Li values of the altered oceanic crust (AOC) (Chan et al. 1992, 2002), depending on whether the rocks gained or lost Li during alteration. The addition of Li from a fluid with δ^7Li similar to that of seawater will lead to higher δ^7Li values in the AOC than in MORB (Bouman et al. 2004; Marschall et al. 2017), whereas the loss of Li from the AOC during dehydration may lower δ^7Li to values lower than those of MORB (Chan et al. 2002). Prograde dehydration of the subducted slab expels fluids and introduces Li into the suprasubduction zone mantle wedge (Marschall et al. 2006; Wunder et al. 2007; Zack et al. 2003), although Li and B contents may be strongly lowered before the slab reaches subarc depths (Leeman et al. 2004). The δ^7Li value of this Li addition to the suprasubduction zone mantle wedge depends on the Li source and on the reaction history of the fluid from the source to the mantle wedge. For instance, orogenic eclogites show a large range of δ^7Li from –21.9 to $+8.2$ ‰ that cannot be explained by isotopic fractionation due to Li loss during dehydration alone (Marschall et al. 2007b), but reflect Li redistribution during the alteration of the protoliths and during subduction and exhumation of the metamorphic rocks.

Lithium redistribution in phengite schists

Dehydration reactions during prograde metamorphism result in the redistribution of Li derived from the consumed phases into (i) newly forming phases, (ii) already present phases, and (iii) a possible fluid phase. Replacement of former hydrous minerals by the growth of minerals of higher thermal stability will redistribute Li, depending on the original Li hosts and the newly formed Li hosts.

For the investigated phengite schists, Li probably was hosted by illite, chlorite (Chl), and chloritoid (Cld) during the initial stages of prograde metamorphism. The breakdown of Ms, Chl and Cld with increasing T and P (e.g. $Cld + Qz + Ms \rightarrow Grt + staurolite + biotite + H_2O$; $Chl + K\text{-feldspar} + Qz \rightarrow Tlc + Ms + H_2O$; $Cld \rightarrow Grt + Ky + H_2O$, Mposkos 1989; Spear and Cheney 1989; Massonne and Schreyer 1989) releases water and redistributes Li. Paragonite has a slightly higher partition coefficient for Li than phengite ($D^{Pg/Phe} = 1.9$, Marschall et al. 2006) and should have higher Li contents than phengite. In the studied phengite schists, however, paragonite has lower Li contents than phengite (Fig. 5A), which illustrates that the Li concentrations of paragonite and phengite are not in equilibrium. Phengite is a peak stage metamorphic mineral. In contrast, paragonite coexists with retrograde albite. Therefore, it indicates that during retrogression most Li was sequestered in phengite.

Similarly, chlorite exhibits a high partition coefficient for Li, with a suggested $D^{Chl/Phe}$ ratio of ~5.2 (Marschall et al. 2006). The average Li contents in chlorite and phengite from samples PhS-5 are 58.4 and 21.4 ppm, respectively. Based on partition coefficients, chlorite should possess a higher Li content (close to 110 ppm). Chlorite formed due to decomposition of garnet during the retrograde metamorphic stage. Phengite formed near peak metamorphic conditions. Thus, the formation of phengite already sequestered a major portion of Li before retrograde chlorite formed. Consequently, late-crystallizing chlorite exhibits lower Li contents than expected from the element partition coefficient (Marschall et al. 2006) between chlorite and phengite.

Mass balance was used to estimate the relative contribution of the various mineral phases to the Li and B budget of the WR samples. The Li (and B) budget for the whole rock samples as estimated from the average contents of the mineral phases did not always agree closely with the measured whole rock contents because of three reasons: (i) Bulk-rock Li and B isotope analyses and Li and B mineral analyses (laser ablation work and phase proportions by point counting) were done on different parts of the same hand-specimen. (ii) If the abundance of a major Li or B host mineral is over- or under-estimated, the calculated budget will deviate from 100%. (iii) The Li and B contents as determined by LA-ICPMS were preferentially obtained

Table 2 Li and B contents and mass balance for the low-*T* and high-*T* eclogites, and phengite schists from the Changning-Menglian orogenic belt

Sample ID	WR or Mineral	Mode	Mean Li	SD	Mean B	SD	WR Li	WR B	Contribution to Li budget	Contribution to B budget
Rock type		%	ppm		ppm		ppm	ppm	%	%
PhS-7 Phengite schist	WR						22	37		
	Ph	30	18.5	2	112	1.3			25.2	90.8
	Chl*	25	58.4	20	9.1	0.4			66.4	6.1
	Grt	15	2.25	1	b.d.l				1.5	
	Qz	20	n.a		n.a					
	Pl	10	n.a		n.a					
PhS-5 Phengite schist	WR						11	17		
	Ph	25	23.3	6.3	54.9	1.5			53.0	80.7
	Chl	7	58.4	19.8	9.1	0.4			37.2	3.75
	Pg	1	8.0	1.4	209	0.3			0.7	12.3
	Grt	15	6.47	5.8	b.d.l				8.8	
	Qz	30	n.a		n.a					
	Pl	20	n.a		n.a					
LTE-7 Gln eclogite	WR						11	6.4		
	Omp	40	22.5	4.8	1.41	0.43			81.8	8.8
	Grt	25	2.02	1.13	b.d.l				4.6	
	Gln	8	18.4	7.9	3.24	1.01			13.4	4
	Ph	15	12.7	6.1	30.9	13.4			17.3	72
	Chl	2	44.6	4.5	1.82	0.6			8.1	0.6
LTE-5 Lws-Ep eclogite	WR						10.3	2.3		
	Omp	50	16.2	1.5	0.96	0.5			78.6	21
	Grt	25	1.55	0.92	b.d.l				3.8	
	Ep	15	0.55	0.57	b.d.l				0.8	
	Ph*	5	12.7	6.1	30.9	13.4			6.2	67.5
	Chl	3	43.5	3.6	4	1.1			12.7	5.2
THE-2 Ky eclogite	WR						25	4.7		
	Omp	50	31.7	6.3	0.87	0.37			63.4	9.3
	Grt	25	1.48	1	b.d.l				1.5	
	Ep	4	6.32	5.4	b.d.l				1	
	Amp	12	25.5	14.6	13.2	5.3			12.2	33.7
	Ms	1	93.5	67.5	305	80			3.7	64.9
THE-1 Grt-Omp eclogite	WR						13	6.9		
	Omp	30	39.4	33.2	1.08	0.3			91	4.7
	Grt	35	0.48	0.63	b.d.l				1.3	
	Amp	15	4.82	1.9	8.73	3.1			5.6	19
	Ms*	2	93.5	67.5	305	80			14.4	88.7
	Pl	10	n.a		n.a					

The samples are not homogeneous. Therefore, the Li and B contents are not homogeneously distributed within and among individual crystals. The calculated Li and B budget for the whole rock samples may deviate from 100% because of three reasons: (i) Bulk-rock Li and B isotope analyses and Li and B mineral analyses (laser ablation work and phase proportions by point counting) were done on different parts of the same hand-specimen. (ii) If the abundance of a major Li or B host mineral is over- or under-estimated, the calculated budget will deviate from 100%. (iii) The Li and B contents as determined by LA-ICPMS were preferentially obtained for large crystals, whereas fine-grained minerals were not probed

Amp amphibole, *Chl* chlorite, *Ep* epidote, *Gln* glaucophane, *Grt* garnet, *Ky* kyanite, *Omp* omphacite, *Ph* phengite, *Pl* plagioclase, *Qz* quartz, *Pg* paragonite, *WR* whole-rock, *b.d.l.* below detection limit, *n.a.* not analyzed

*The Li and B contents for marked minerals are based on data from the same rock types, as they are heterogeneously distributed in the sample. The mineral mode for each sample is not 100% as the rocks also contain quartz, rutile, lawsonite, titanite, sulfides, and/or carbonate minerals that have not been included in the calculation of the Li and B budget

for large crystals, whereas fine-grained minerals were not probed. Despite these limitations, the mass balance clearly shows which minerals dominate the Li and B budgets of the various rocks. For instance, according to mass balance calculations, phengite contributes approximately $25-53\%$ of the Li budget of metapelitic whole-rock samples (Table 2). As phengite in mica schists may remain stable from blueschist facies conditions to high-grade conditions reaching more than 4.0 GPa and 800 °C (Schmidt et al. 2004), mica schists could transport a significant portion of their Li budget into the lithospheric mantle.

Lithium redistribution in low-T eclogites

For low-*T* eclogites (Gln eclogites and Lws-Ep eclogites), dehydration of lawsonite and chlorite from blueschist to eclogite facies follows the reactions $Lws + Chl \pm Pg \rightarrow Grt + Omp + Gln \pm Tlc + H_2O$ and $Lws + Gln + Tlc \rightarrow Grt + Omp + H_2O$. Lithium originally hosted in chlorite was lost into dehydration fluids, and in part may have been incorporated into glaucophane and omphacite. The breakdown of lawsonite and glaucophane releases water during prograde metamorphism, which may transport Li into adjacent rocks or the mantle wedge. Omphacite, the mineral with the highest modal proportion in the low-*T* eclogite samples, has relatively high Li contents (9.1–28.6 ppm) (Fig. 5C and D). Therefore, the Li budget of low-*T* eclogites is dominated by omphacite (Table 2). Although phengite and glaucophane have high Li contents of up to 35.6 ppm, they do not contribute a lot to the whole rock budget due to their low modal abundances (Table 2). The Li concentrations and δ^7Li values of the low-*T* eclogite samples fall far from the compositional fields of MORB and AOC end members (Fig. 7A,B, Marschall et al. 2017), and δ^7Li values are not systematically decreased in samples with lower Li contents (Fig. 7B). Instead, the Li contents and δ^7Li values of the low-*T* eclogite samples plot in the same range as the phengite schists (Fig. 7B). As the low-*T* eclogites form lenses or layers within the phengite schists, Li was probably transferred from the schists into the eclogites. Lithium could be added from the schists to the low-*T* eclogite samples during prograde and/or retrograde metamorphism. Because the peak mineral phase (omphacite) controls the Li budget (Fig. 5C and D), Li from the phengite schists probably was added to the eclogites before omphacite formed, i.e., during prograde metamorphism. Amphibolitized eclogites have similar Li contents and δ^7Li values as fresh low-*T* eclogites (Fig. 7B), reflecting little change in the Li budget and isotopic composition during retrogression.

Lithium redistribution in high-T eclogites

The peak mineral assemblages of high-*T* eclogites (Grt-Omp eclogites and Ky eclogites) include garnet and omphacite, as well as minor kyanite, rutile, and magnesite. In addition, there is some retrograde amphibole and muscovite (Fig. 3F and G). The Li budget for the whole rock samples is dominated by omphacite (Table 2), whereas Li contributions from garnet, kyanite, and epidote are negligible (Fig. 5E and F). Omphacite contributes about 60–90% to the whole-rock Li budget, while retrograde amphibole and muscovite contribute 3.7–14.4% to the Li budget. Amphibole has similar or lower Li contents than omphacite (Table 2), which implies that little or no Li was added to the high-*T* eclogites during exhumation. The high-*T* eclogites have low δ^7Li values (-13.2 to -5.8 ‰), much lower than the phengite schists (Fig. 7B). Lithium released from the precursor rocks of eclogites during prograde reactions in part may have partitioned between fluids and omphacite, allowing for some loss of Li (Fig. 3G, $Grt + Czo + Qz \rightarrow Ky + Omp + H_2O$), and in part was locally redistributed during water-absent reaction ($Di + Pl \rightarrow Grt + Qz$) (Bucher and Grapes 2011). The difference in δ^7Li between low-*T* and high-*T* eclogites reflects mainly their contrasting fluid-rock interaction histories during prograde metamorphism. The protoliths of high-*T* eclogites lost significant amounts of Li during water–rock interaction, resulting in lower δ^7Li values before subduction. The Li isotope data indicate that low-*T* and high-*T* eclogites have experienced different degrees of Li loss during near-surface alteration and prograde metamorphism. The high-*T* eclogites have Li isotopic compositions contrasting with those of phengite schists (Fig. 7B), which indicates that the high-*T* eclogites were tectonically brought in contact with the phengite schists after passing the metamorphic peak. Otherwise, high-*T* eclogites should have δ^7Li values similar to the phengite schists and low-*T* eclogites.

Boron redistribution and isotopic fractionation during high-pressure metamorphism and exhumation

Boron isotopic behavior in the subduction zones

Subduction is an important process for transporting B with a broad range of isotopic compositions into the asthenospheric mantle (De Hoog et al. 2018; Palmer 2017). The B content of the upper mantle is estimated to be 0.1–0.2 ppm, whereas concentrations in the crust are two to three orders of magnitude higher (Spivack 1986). The distributions of B and $\delta^{11}B$ are controlled by a dynamic cycle, including weathering, uptake of B by sediments and oceanic crust,

subduction, and devolatilization of the subducted rocks (Smith et al. 1995). Modern seawater has a high B content (30 to 36.8 ppm) and $\delta^{11}B$ value ($+39.61 \pm 0.04$ ‰) (Spivack and Edmond 1987; Foster et al. 2010). Fresh MORB has low B contents (0.077 ± 0.01 ppm) and $\delta^{11}B$ values (-7.1 ± 0.9 ‰) (Marschall et al. 2017). Absorption and incorporation of seawater B in secondary minerals of altered oceanic crust and sediments increase the B contents and the $\delta^{11}B$ values of the altered rocks (Williams et al. 2001). Subduction of these rocks introduces B into the mantle, whereby B released from the slab has higher $\delta^{11}B$ values than B remaining in the slab (Benton et al. 2001; Cannaò et al. 2023; Konrad-Schmolke and Halama 2014; Pabst et al. 2012). Because of this change in the B isotopic composition with B loss, boron concentrations and $\delta^{11}B$ values of fluids released from the slab may vary with depth (e.g. Leeman et al. 2004). In addition to prograde B redistribution, B in eclogites may also be redistributed or added from wall rocks during exhumation (Bebout and Nakamura 2003).

Boron redistribution in phengite schists

The phengite schist samples have B contents ranging from 6.8 to 86 ppm. The majority of samples show consistently low $\delta^{11}B$ values of -9.5 to -14.4 ‰ (Table S1). Boron was initially hosted in clay minerals and micas in the protoliths of the phengite schists. During prograde metamorphism, the breakdown of clay minerals and, later on, the conversion of early-metamorphic muscovite to phengite releases B for redistribution between minerals and fluids (Hacker 2008; Nakano and Nakamura 2001; Romer and Meixner 2014). Phengite can sequester B released during prograde muscovite- and chlorite-dehydration in the schists. Mass balance calculations indicate that phengite contributes 80–90% to the whole rock B budget (Fig. 5A,B and Table 2). Major loss of B during subduction dehydration may significantly decrease the $\delta^{11}B$ values and could account for the extremely low $\delta^{11}B$ value of -22.8 ‰ in sample PhS-6 (Fig. 7C). One sample (PhS-3) has a $\delta^{11}B$ value similar to that of as amphibolitized eclogite RE-4 (Fig. S2), possibly indicating that these rocks interacted with similar fluids during retrograde metamorphism.

The estimated $D^{\text{Phe/Pg}}$ ratio for B is approximately 0.46 (Marschall et al. 2006). In sample PhS-5, paragonite (av. 209 ppm) shows much higher B contents than phengite (av. 55 ppm). This discrepancy indicates that the contents of B in phengite and retrograde paragonite have not equilibrated, which is in line with the Li distribution pattern (Fig. 8). The formation of paragonite during decompression, along with its heterogeneously distributed boron (Fig. 8) may reflect variable availability of B during retrograde mineral growth.

Boron redistribution in low-*T* eclogites

In the low-*T* eclogites, phengite is the major B sequestering phase (Fig. 5C and D; Table 2). Glaucophane and omphacite have low B contents (av. < 3.5 ppm). Garnet and epidote commonly have B contents below the limit of detection (Table S2), therefore, these two minerals are considered negligible for the B budgets of the bulk rocks. The B contents in the rocks decrease along with the contents of K_2O, Rb, and Cs (Fig. 6), indicating that phengite dominates the B as well as the K_2O and LILE budgets of the whole rock samples. A modal contribution of 5% phengite accounts for 68% of the B budget of the whole rock sample (Table 2). The calculated bulk-rock budgets of B of some low-*T* eclogites are lower than the measured bulk-rock concentrations (Table 2), possibly reflecting the heterogeneous distribution of phengite, and retrograde chlorite, which locally is a significant host of B (and Li) in this sample (LTE-5). Low-*T* eclogites have lower $\delta^{11}B$ values (-15.1 to -8.1 ‰; Table 2) than MORB (-2.2 to -9.4 ‰, av. $=-7.1 \pm 0.9$ ‰) and AOC ($+0.8 \pm 0.2$ ‰; Marschall et al. 2017), but fall within the $\delta^{11}B$ range of the phengite schists (Fig. 7D). Most low-*T* eclogite samples fall in a narrow range of $\delta^{11}B$ values (-11.5 to -8.1 ‰; Table 2) independent of B concentrations. Only one of these samples (LTE-8) has a lower $\delta^{11}B$ value (-15.1 ‰; Fig. 7C). This sample has lower TiO_2 and LREE, and higher MgO, K_2O, Rb, Cs and Pb contents (Fig. 6 and Fig. S1) than the other low-*T* eclogite samples, reflecting a slightly different protolith chemistry. Thus, the lower $\delta^{11}B$ values of these sample may reflect heterogeneous $\delta^{11}B$ of the protolith or a fluid that added B with locally variable $\delta^{11}B$. The B budgets and B isotopic compositions of the low-*T* eclogites, analogous to the Li budget and the Li isotopic compositions (Fig. 7D), are strongly affected by the infiltration of fluids derived from wall-rock phengite schists that also resulted in LILE enrichment (Fig. S1).

Boron redistribution in high-*T* eclogites

The high-*T* eclogites have similar B and $\delta^{11}B$ ranges as the low-*T* eclogites. Amphibole and muscovite are the major B hosts, contributing as much as 90% to the whole-rock B budget (Fig. 5E and F; Table 2). Garnet and omphacite have low B concentrations, commonly less than 2 ppm (Fig. 5E and F). As amphibole and muscovite formed during retrogression, B is likely to have been added by ingressing fluids during exhumation. This inference is in line with some of the retrograde amphibolitized eclogites having higher B contents (1.6 to 19.0 ppm) than fresh low-*T* eclogites (0.8 to 7.9 ppm) (Fig. 7C).
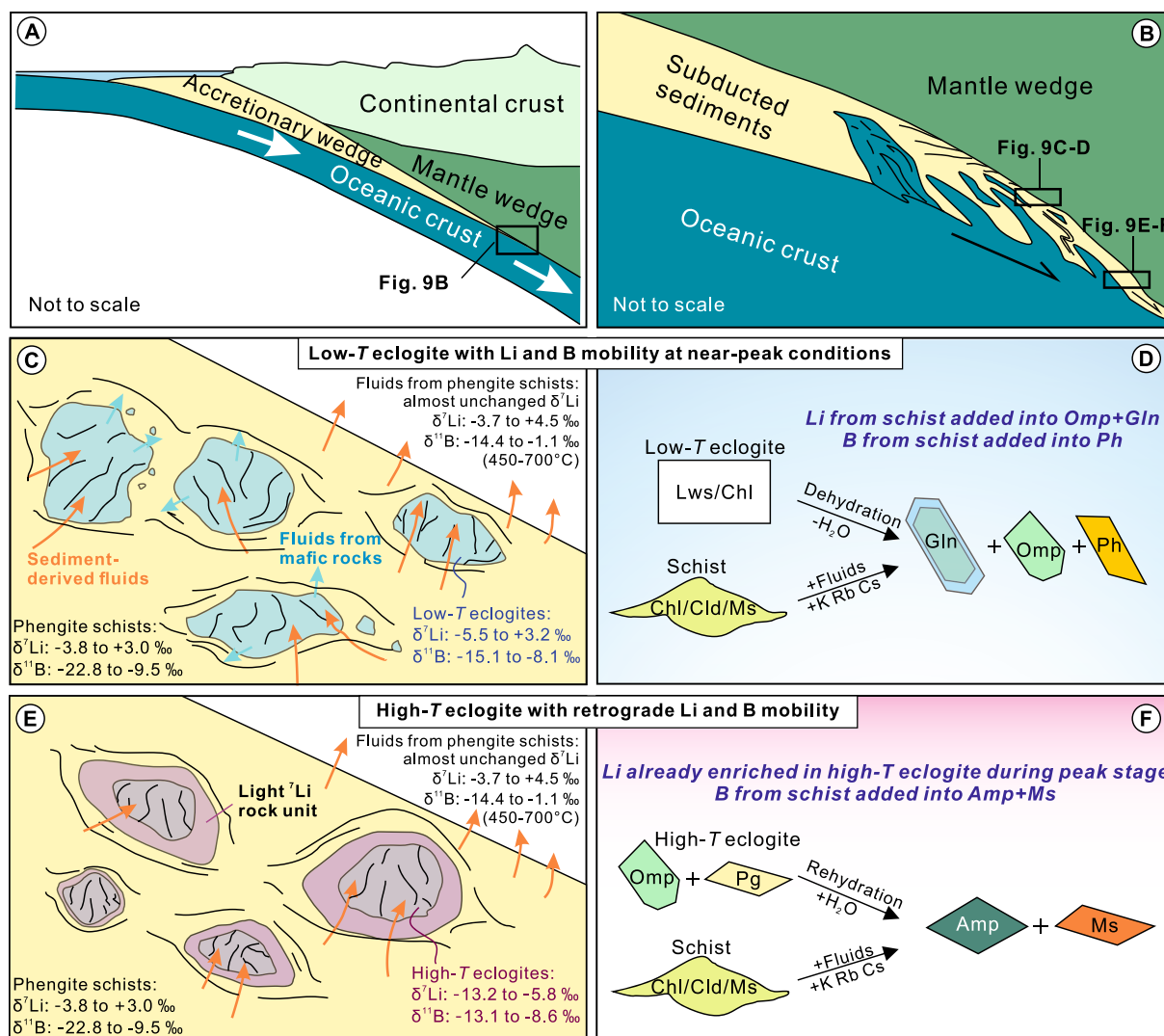
Fig. 9 Schematic diagram of Li and B sources and sinks during the subduction in the Changning-Menglian suture zone. **A–B** Slivers of subducted oceanic crust became sheared off from the downgoing slab and form, together with metasedimentary cover units, a subduction channel mélange. The low-*T* and high-*T* eclogites were brought in contact with the phengite schists at different depths (see Fig. 2). The low-*T* eclogites were brought in contact during the prograde metamorphism or near-peak conditions. In contrast, the high-*T* eclogites were brought in contact with the phengite schists during the retrograde metamorphism. Lithium and B lost from phengite schists during high-*P* metamorphism have two kinds of sinks: (i) Li and B may be taken up by eclogite blocks brought in contact with the schists in the mélange zone or (ii) Li and B may be lost to the mantle wedge. **C–F** Schematic diagram showing Li and B exchange in major mineral phases during peak-stage and retrograde metamorphism. **C–D** Gln and Omp were probably formed when Lws-breakdown released major amounts of water at prograde or near-peak metamorphic stage (Lws + Chl ± Pg → Grt + Omp + Gln ± Tlc + H$_2$O and Lws + Gln + Tlc → Grt + Omp + H$_2$O). Because Omp and Gln are the major Li host in the low-*T* eclogites, Li from the phengite schists must have been added to the eclogites during near-peak metamorphism. **E–F** High-*T* eclogites have experienced amphibolite facies overprint. Retrogression-related amphibole and muscovite carry additional B that was released from the phengite schist. Abbreviations are the same as in Fig. 2

Sources and sinks for mobile Li and B

Lithium and B lost from the phengite schists during high-*P* metamorphism in subduction zones may escape to (i) the adjacent eclogites or (ii) the mantle wedge (Fig. 9). Dehydration of phengite schists would likely produce fluids with higher δ^{7}Li and δ^{11}B values than the source rocks, as ^{7}Li and ^{11}B partition preferentially into the fluid (Wunder et al. 2005, 2007) according to the equations Δ^7Li$_{\text{mica-fluid}}$ = − 4.52 × (1000/T [K]) + 4.74 (Eq. (1), Wunder et al. 2007) and Δ^{11}B$_{\text{solid/melt-fluid}}$ = − 10.69 × (1000/T [K]) + 3.88 (Eq. (2), Wunder et al. 2005). The temperature range of 450–700 °C of the phengite schists was used to calculate the Δ^7Li and Δ^{11}B. At these temperatures,

$\Delta^7\text{Li}_{\text{solid-fluid}}$ is relatively small, ranging from -1.5 to 0.1 (Wunder et al. 2007). Similarly, $\Delta^{11}\text{B}_{\text{solid-fluid}}$ for this temperature range is -10.0 to -6.6 for $[3]_{\text{fluid}}$ and $[4]_{\text{solid}}$ coordination (Wunder et al. 2005). The measured $\delta^7\text{Li}$ and $\delta^{11}\text{B}$ values of phengite schists vary from -3.8 to $+3.0$ ‰ and -22.8 to -9.5 ‰. Therefore, the calculated ranges of $\delta^7\text{Li}$ values of the released fluids in the temperature range of 450–700 °C can be expected to be about -3.7 to $+4.5$ ‰ based on Eq. (1). Similarly, the calculated $\delta^{11}\text{B}$ values of fluids released from the phengite schists fall in the ranges -11.9 to $+1.4$ ‰ for 450 °C and -15.7 to -2.4 ‰ for 700 °C (Eq. (2), Fig. 9C and E).

Lithium and B lost from the phengite schists and trapped in eclogites

The fluids released from the phengite schists and transported into the eclogite lenses during either prograde or retrograde metamorphism (Fig. 9A–F) will significantly influence the contents and isotopic compositions of Li and B in eclogites. Lithium in low-*T* eclogites is mainly hosted in omphacite (Fig. 5C and D; Table 2). Based on the equation $\Delta^7\text{Li}_{\text{clinopyroxene-fluid}} = -4.61 \times (1000/T\,[\text{K}]) + 2.48$ (Wunder et al. 2006), the recrystallized omphacite would have a $\delta^7\text{Li}$ value that is 2.8 δ units lower than the $\delta^7\text{Li}$ value of fluids at 600 °C. The observed $\delta^7\text{Li}$ values of the low-*T* eclogites (-5.5 to $+3.2$ ‰) overlap with the calculated $\delta^7\text{Li}$ values of the fluids from the phengite schists (-3.8 to $+3.0$ ‰). The overlapping $\delta^7\text{Li}$ ranges indicate that Li released from phengite schists could have been sequestered in glaucophane and omphacite in the low-*T* eclogites during prograde or peak metamorphism (Fig. 9D), which would imply that the low-*T* eclogites formed lenses and blocks in the phengite schists during the formation of the omphacite-bearing peak-mineral assemblage (Fig. 9A–D).

The low $\delta^7\text{Li}$ values of the mafic eclogites reflect the transfer of Li from the sediments into eclogites at depth. In tectonic mélanges, as for instance in the Franciscan area, rigid blocks of mafic crust may have been exposed against a wide range of ductile wall rocks along their $P - T$ loop (e.g. Ernst 2016; Federico et al. 2007). Therefore, the lower $\delta^7\text{Li}$ values of the high-*T* eclogites compared to their present wall-rocks (Fig. 7B) do not argue against an exchange with the wall rocks, but simply imply there was exchange with different wall rocks with lower $\delta^7\text{Li}$ values than the present ones. Very low $\delta^7\text{Li}$ values are known from crustal rocks and may be the combined results from two different processes that lower $\delta^7\text{Li}$. These processes include (i) intense chemical weathering on the continent (e.g. Qiu et al. 2009) and (ii) fluid and Li loss during sediment compaction, diagenesis, and prograde metamorphism (e.g. Chan et al. 1994; Marschall et al. 2007b). As clay-rich sediments and their metamorphic equivalents may have relatively high Li

contents (e.g. Chan et al. 1994; Teng et al. 2004; Romer et al. 2014), already minor Li contributions from pelitic rocks to the high-*T* eclogites may dominate the Li budget of the eclogites.

The high-*T* eclogites have higher Li contents compared to MORB (Fig. 7B), indicating the addition of Li into the high-*T* eclogites. Differences in lithium content are associated with mineral growth during different metamorphic stages, influenced by fluids that are derived from or interacted with the various wall rocks. High-*T* eclogites likely incorporated Li during prograde metamorphism, given that the peak stage mineral, omphacite, hosts the majority of Li in these rocks. While some Li may have been added during retrograde metamorphism, amphibole (the main retrograde phase) does not contribute significantly to the whole rock Li budget (< 12.2%, Table 2). Consequently, the $\delta^7\text{Li}$ signature acquired during prograde metamorphism was largely preserved in high-*T* eclogites.

Redistribution of B in the eclogites differs from the redistribution of Li, as B is hosted in amphibole and muscovite rather than in glaucophane and omphacite. The partially retrogressed high-*T* eclogites have elevated B contents, which were introduced from the phengite schists during the replacement of omphacite by amphibole (Fig. 9F). The results of mixing modeling suggest that an approximate 10% addition of B from mica schists to the protoliths of the low-*T* and high-*T* eclogites can account for the observed B contents and $\delta^{11}\text{B}$ values of these metamorphic rocks (Fig. 7C). As Li and B are hosted in different mineral phases in our samples (peak vs. retrograde minerals), the contents and isotopic compositions of Li and B became decoupled during subduction-related fluid-mediated redistribution.

Lithium and B lost from the phengite schists to the mantle wedge

The fluids released from the phengite schists do not only interact with the enclosed mafic eclogite units but may also enter the mantle wedge (Fig. 9A,B), where they react with mantle peridotites to form pyroxenite veins and amphibole- or phlogopite-bearing veins (Foley 1992; Prelević et al. 2012; Soder and Romer 2018). During this metasomatism, Li is partitioned into olivine, clinopyroxene, amphibole, and phlogopite, whereas B may be hosted in phlogopite and amphibole. This process eventually leads to a wide range of $\delta^7\text{Li}$ and $\delta^{11}\text{B}$ values on any spatial scale in the mantle wedge, depending on the source of the fluids (different lithologies) and the relative contributions of these additions and of the ambient mantle to the Li and B budgets of the metasome. Magmas from partial melting of the metasomatized mantle inherit dominantly the Li and B isotopic signature of the metasomatized mantle domains, especially for low degrees of partial melting as typical for

lamproitic, lamprophyric, shoshonitic, and alkaline magmas (Abdelfadil et al. 2014; Agostini et al. 2008; Hao et al. 2022; Sugden et al. 2020; Wang et al. 2020c).

Subducted hydrated oceanic crust and serpentinites are regarded as the most important sources of B in magmatic arc rocks that may show a shift toward lower $\delta^{11}B$ values at greater distance from the trench (Savov et al. 2005, 2007; Pabst et al. 2011, 2012; Scambelluri and Tonarini 2012; Martin et al. 2016). This shift can reflect progressive loss of B from the subducted rocks (e.g. Rosner et al. 2003; Konrad-Schmolke and Halama 2014; Liu et al. 2022). The large range of $\delta^{11}B$ values of arc magmas (– 9.5 to + 16 ‰; De Hoog and Savov 2018), however, may not solely be controlled by fractionation during B loss, but also may reflect different sources and may be related to the stability of phases that sequester B. For instance, serpentine may fix a significant portion of boron in the forearc domain of a subduction system, and release it at greater depth to the mantle when the stability of serpentine is surpassed (De Hoog and Savov 2018; Martin et al., 2016). Boron with low $\delta^{11}B$ values also may be introduced into the mantle via subducted sediments, such as the studied phengite schists that have high B contents (6.8 to 86.0 ppm, av. 31.9 ppm) and low $\delta^{11}B$ values (– 9.5 to – 22.8‰, av. – 13.6 ‰). Due to the high stability of phengite, sedimentary materials may have a limited impact on the B contents and isotopic compositions of the forearc mantle wedge. At greater depths, however, the decomposition of phengite may release B into the mantle. Both serpentine and phengite may carry isotopically light B into the mantle as observed for some mantle-derived magmas from subduction and collision zones (Hao et al. 2022; Zhang et al. 2023; Luciani et al. 2023).

Contrasting Li and B in eclogites

Blueschists and oceanic eclogites from other orogenic belts show large ranges of Li contents (1.0 to 94.4 ppm) and Li isotopic compositions ($\delta^7Li = -$ 12.9 to + 4.6 ‰; Fig. 10A), which is inconsistent with the small ranges for Li and δ^7Li obtained from modeling oceanic subduction (Marschall et al. 2007b). High-*P* eclogites of the current study significantly exchanged Li with their metasedimentary wall rocks during prograde subduction, largely adjusting to the Li isotopic compositions of their wall rocks. Thus, the observed large δ^7Li range in eclogites predominantly reflects the contrasting Li signatures of the wall rocks.

In a similar way, high-*P* eclogites worldwide may have exchanged B with their wall rocks during retrogression, explaining both the significant variations in B content (0.9 to 55.5 ppm) and B isotopic composition ($\delta^{11}B = -$ 12.0 to + 8.8 ‰; Fig. 10B). For instance, eclogites that were exhumed in a serpentinite matrix are likely to have elevated
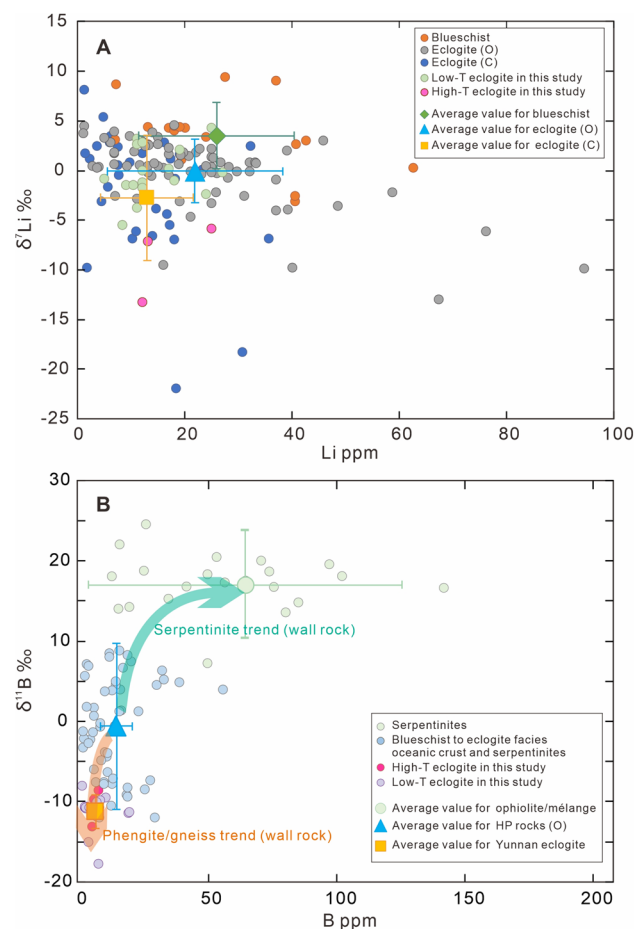

Fig. 10 Compilation of whole rock (WR) Li and B concentration and isotope data of high-pressure mafic rocks and serpentinites from various orogenic belts. **A** Li [ppm] vs. δ^7Li. **B** B [ppm] vs. $\delta^{11}B$. Data from Cannaò et al. 2016; Halama et al. 2011; Liu et al. 2019; Marschall et al. 2007b; Penniston-Dorland et al. 2010; Simons et al. 2010; Yamada et al. 2019; Zack et al. 2003 and this study. Li concentrations and isotopic ratios in blueschists and eclogites show a large range of Li = 0.99 to 94.4 ppm and $\delta^7Li = -$ 12.9 to + 4.6 ‰. The eclogites that were exhumed along with serpentinites show elevated B contents and $\delta^{11}B$ values. The different Li and B characteristics in different wall rocks (such as the phengite schist trend [orange line] and serpentinite trend [green line]) lead to highly variable Li and B signatures in the exhumed eclogites. *O* oceanic, *C* continental

B contents and $\delta^{11}B$ values, as serpentinites that were formed upon interaction of oceanic lithosphere with seawater commonly have high B contents and $\delta^{11}B$ values (av. 65.3 ppm, + 16.9 ‰; Cannao et al. 2015; Halama et al. 2011; Harvey et al. 2014; Liu et al. 2019; Marschall et al. 2007b; Penniston-Dorland et al. 2010; Simons et al. 2010; Yamada et al. 2019; Zack et al. 2003) (Fig. 10B). In contrast, eclogite blocks within felsic gneisses and schists would tend to have low B contents (< 10 ppm) and low $\delta^{11}B$ values (Fig. 10B).

The contrasting Li and B characteristics in different wall rocks (schists vs. serpentinites) may account for the

contrasting Li and B signatures in the exhumed blueschists and eclogites. The timing of isotopic exchange between eclogites and their wall rocks during prograde or retrograde processes is essential for the contents and isotopic compositions of Li and B in blueschists and eclogites. In the studied samples, Li addition to the eclogites most likely represents exchange with wall rocks during prograde metamorphism, whereas the boron isotopic composition of the eclogites records B exchange with wall rocks during exhumation (Cannaò et al. 2023). In tectonic mélanges, tectonic blocks of high-grade metamorphic rocks in ductile host rocks of similar or lower metamorphic grade may have been in contact with a wide range of different wall rocks during their *P–T* loop (e.g. Ernst 2016; Federico et al. 2007), which in turn implies that Li and B introduced from the wall rocks into these blocks may be derived from different protoliths.

Conclusions

Low-*T* and high-*T* eclogites have different Li and B isotopic compositions largely reflecting the mineralogical control on the loss and gain of Li and B during prograde and/or retrograde metamorphism and the exchange of Li and B with the immediate wall rocks. If the wall rocks, as for instance phengite schists, have higher Li and B contents than the subducted mafic rocks, this exchange results in an overall Li and B addition to the mafic rocks combined with a shift of the Li and B isotopic compositions toward the wall rock compositions. In the low-*T* eclogites, the peak metamorphic minerals omphacite and glaucophane are the main Li hosts. The low-*T* eclogites have higher Li contents than typical basalts, which indicates that Li has been added. The Li isotopic compositions of low-*T* eclogite samples fall in the same range as phengite schist wall rocks, i.e. δ^7Li values of -5.5 to $+3.2$ ‰, indicating that Li added to the eclogites was derived from phengite schists. The budget and isotopic compositions of B are affected by the infiltration of fluids derived from phengite schists during prograde or near-peak metamorphism, as the δ^{11}B values (-15.1 to -8.1 ‰) overlap with those of the phengite schists.

The high-*T* eclogites have much lower δ^7Li values (-13.2 to -5.8 ‰) than the phengite schists (-3.8 to $+3.0$ ‰), reflecting prograde loss of Li or exchange with wall rocks characterized by low δ^7Li values. As retrograde amphibole and muscovite contribute only little to the Li budget of the rock, but are the major B host of the retrogressed eclogites, post-peak additions of fluids from the phengite schists have no effect on the Li contents and isotopic composition of the rock, but shift δ^{11}B toward the values of the phengite schists.

Lithium and B lost from the phengite schists during prograde metamorphism have two major sinks: mafic rocks enclosed in the schists (preserved as lenses or blocks of eclogites) and the mantle wedge where the lost fluids induce metasomatism by forming pyroxenite veins and amphibole- or phlogopite-bearing veins. Prograde dehydration of phengite schists (-22.8 and -9.5 ‰) would introduce light B into the mantle wedge and this B may be incorporated in magmas derived from the metasomatized lithospheric mantle. The contrasting Li and B isotopic signatures observed in the eclogites are likely caused by the fluid exchange with different types of wall rocks during prograde metamorphism and exhumation.

References

Abdelfadil KM, Romer RL, Glodny J (2014) Mantle wedge metasomatism revealed by Li isotopes in orogenic lamprophyres. Lithos 196–197:14–26. https://doi.org/10.1016/j.lithos.2014.02.021

Agostini S, Ryan JG, Tonarini S, Innocenti F (2008) Drying and dying of a subducted slab: coupled Li and B isotope variations in Western Anatolia Cenozoic Volcanism. Earth Planet Sci Lett 272:139–147. https://doi.org/10.1016/j.epsl.2008.04.032

Andrews E, Pogge von Strandmann PAE, Fantle MS (2020) Exploring the importance of authigenic clay formation in the global Li cycle. Geochim Cosmochim Acta 289:47–68. https://doi.org/10.1016/j.gca.2020.08.018

Barnes JD, Cullen J, Barker S, Agostini S, Penniston-Dorland S, Lassiter JC, Klügel A, Wallace L (2019) The role of the upper plate in controlling fluid-mobile element (Cl, Li, B) cycling through subduction zones: Hikurangi forearc, New Zealand. Geosphere 15:642–658. https://doi.org/10.1130/GES02057.1

Bebout GE, Barton MD (1989) Fluid flow and metasomatism in a subduction zone hydrothermal system: catalina Schist terrane, California. Geology 17:976–980. https://doi.org/10.1130/0091-7613(1989)017/3C0976:FFAMIA/3E2.3.CO;2

Bebout GE, Nakamura E (2003) Record in metamorphic tourmalines of subduction-zone devolatilization and boron cycling. Geology 31:407–410. https://doi.org/10.1130/0091-7613(2003)031/3C0407:RIMTOS/3E2.0.CO;2

Bebout GE, Penniston-Dorland SC (2016) Fluid and mass transfer at subduction interfaces—The field metamorphic record. Lithos 240–243:228–258. https://doi.org/10.1016/j.lithos.2015.10.007

Benton LD, Ryan JG, Tera F (2001) Boron isotope systematics of slab fluids as inferred from a serpentine seamount, Mariana forearc. Earth Planet Sci Lett 187:273–282. https://doi.org/10.1016/S0012-821X(01)00286-2

Benton LD, Ryan JG, Savov IP (2004) Lithium abundance and isotope systematics of forearc serpentinites, Conical Seamount, Mariana forearc: insights into the mechanics of slab-mantle exchange during subduction. Geochem Geophys Geosyst. https://doi.org/10.1029/2004GC000708

Bouman C, Elliott T, Vroon PZ (2004) Lithium inputs to subduction zones. Chem Geol 212:59–79. https://doi.org/10.1016/j.chemgeo.2004.08.004

Bucher K, Grapes R (2011) Petrogenesis of metamorphic rocks. Springer-Verlag, Berlin Heidelberg

Cannaò E, Agostini S, Scambelluri M, Tonarini S, Godard M (2015) B, Sr and Pb isotope geochemistry of high-pressure Alpine metaperidotites monitors fluid-mediated element recycling during serpentinite dehydration in subduction mélange (Cima di Gagnone, Swiss Central Alps). Geochim Cosmochim Acta 163:80–100. https://doi.org/10.1016/j.gca.2015.04.024

Cannaò E, Scambelluri M, Agostini S, Tonarini S, Godard M (2016) Linking serpentinite geochemistry with tectonic evolution at the subduction plate-interface: The Voltri Massif case study (Ligurian Western Alps, Italy). Geochim Cosmochim Acta 190:115–133. https://doi.org/10.1016/j.gca.2016.06.034

Cannaò E, Scambelluri M, Müntener O, Putlitz B, Agostini S (2023) Inheritance versus subduction-related $\delta^{11}B$ signatures of eclogites: insights from the Voltri Massif (Ligurian Western Alps, Italy). Chem Geol 61:121218. https://doi.org/10.1016/j.chemgeo.2022.121218

Chan LH, Edmond JM, Thompson G, Gillis K (1992) Lithium isotopic composition of submarine basalts: implications for the lithium cycle in the oceans. Earth Planet Sci Lett 108:151–160. https://doi.org/10.1016/0012-821X(92)90067-6

Chan LH, Gieskes JM, You CF, Edmond JM (1994) Lithium isotope geochemistry of sediments and hydrothermal fluids of the Guaymas Basin, Gulf of California. Geochim Cosmochim Acta 58:4443–4454. https://doi.org/10.1016/0016-7037(94)90346-8

Chan LH, Leeman WP, You CF (2002) Lithium isotopic composition of Central American volcanic arc lavas: implications for modification of subarc mantle by slab-derived fluids: correction. Chem Geol 182:293–300. https://doi.org/10.1016/S0009-2541(01)00298-4

Catanzaro EJ, Champion CE, Garner EL, Marinenko G, Sappenfield KM, Shields WR (1970) Boric acid: isotopic and assay standard reference materials. NBS (US) Spec Publ, pp 1–71

Conticelli S, Guarnieri L, Farinelli A, Mattei M, Avanzinelli R, Bianchini G, Boari E, Tommasini S, Tiepolo M, Prelević D, Venturelli G (2009) Trace elements and Sr–Nd–Pb isotopes of K-rich, shoshonitic, and calc-alkaline magmatism of the Western Mediterranean Region: Genesis of ultrapotassic to calc-alkaline magmatic associations in a post-collisional geodynamic setting. Lithos 107:68–92. https://doi.org/10.1016/j.lithos.2008.07.016

De Hoog JCM, Savov IP (2018) Boron isotopes as a tracer of subduction zone processes. In: Foster G, Marschall H (eds) Boron Isotopes: The Fifth Element. Springer International Publishing, Cham, pp 217–247

Deng J, Wang C, Zi JW, Xia R, Li Q (2018) Constraining subduction-collision processes of the Paleo-Tethys along the Changning-Menglian Suture: new zircon U-Pb ages and Sr–Nd–Pb–Hf–O isotopes of the Lincang Batholith. Gondwana Res 62:75–92. https://doi.org/10.1016/j.gr.2017.10.008

Ernst W (2016) Franciscan mélanges: coherent blocks in a low-density, ductile matrix. Int Geol Rev 58:626–642. https://doi.org/10.1080/00206814.2015.1108879

Fan W, Wang Y, Zhang Y, Zhang Y, Jourdan F, Zi J, Liu H (2015) Paleotethyan subduction process revealed from Triassic blueschists in the Lancang tectonic belt of Southwest China. Tectonophysics 662:95–108. https://doi.org/10.1016/j.tecto.2014.12.021

Federico L, Crispini L, Scambelluri M, Capponi G (2007) Ophiolite mélange zone records exhumation in a fossil subduction channel. Geology 35:499–502. https://doi.org/10.1130/G23190A.1

Flesch GD, Anderson AR, Svec HJ (1973) A secondary isotopic standard for $^6Li/^7Li$ determinations. Int J Mass Spectrom Ion Proc 12:265–272. https://doi.org/10.1016/0020-7381(73)80043-9

Foley S (1992) Petrological characterization of the source components of potassic magmas: geochemical and experimental constraints. Lithos 28:187–204. https://doi.org/10.1016/0024-4937(92)90006-K

Foster G, Pogge von Strandmann P, Rae J (2010) Boron and magnesium isotopic composition of seawater. Geochem Geophys Geosyst. https://doi.org/10.1029/2010GC003201

Govindaraju K, Potts PJ, Webb PC, Watson JS (1994) 1994 report on Whin Sill Dolerite WS-E from England and Pitscurrie Microgabbro PM-S from Scotland: assessment by one hundred and four international laboratories. Geostand Newsl 18:211–300. https://doi.org/10.1111/j.1751-908X.1994.tb00520.x

Hacker BR (2008) H$_2$O subduction beyond arcs. Geochem Geophys Geosyst 9:Q03001. https://doi.org/10.1029/2007GC001707

Halama R, John T, Herms P, Hauff F, Schenk V (2011) A stable (Li, O) and radiogenic (Sr, Nd) isotope perspective on metasomatic processes in a subducting slab. Chem Geol 281:151–166. https://doi.org/10.1016/j.chemgeo.2010.12.001

Hao LL, Wang Q, Kerr AC, Wei GJ, Huang F, Zhang MY, Qi Y, Ma L, Chen XF, Yang YN (2022) Contribution of continental subduction to very light B isotope signatures in post-collisional magmas: evidence from southern Tibetan ultrapotassic rocks. Earth Planet Sci Lett 584:117508. https://doi.org/10.1016/j.epsl.2022.117508

Harvey J, Garrido CJ, Savov I, Agostini S, Padrón-Navarta JA, Marchesi C, Sánchez-Vizcaíno VL, Gómez-Pugnaire MT (2014) ^{11}B-rich fluids in subduction zones: the role of antigorite dehydration in subducting slabs and boron isotope heterogeneity in the mantle. Chem Geol 376:20–30. https://doi.org/10.1016/j.chemgeo.2014.03.015

Ishikawa T, Nakamura E (1994) Origin of the slab component in arc lavas from across-arc variation of B and Pb isotopes. Nature 370:205–208. https://doi.org/10.1038/370205a0

Jian P, Liu D, Kröner A, Zhang Q, Wang Y, Sun X, Zhang W (2009) Devonian to Permian plate tectonic cycle of the Paleo-Tethys Orogen in southwest China (I): geochemistry of ophiolites, arc/back-arc assemblages and within-plate igneous rocks. Lithos 113:748–766. https://doi.org/10.1016/j.lithos.2009.04.006

Jin XC, Wang ZY, Xie GL (2003) Devonian to Triassic successions of the Changning-Menglian Belt, Western Yunnan, China. Acta Geol Sin-Engl Ed 77:440–456. https://doi.org/10.1111/j.1755-6724.2003.tb00125.x

Jochum KP, Willbold M, Raczek I, Stoll B, Herwig K (2005) Chemical characterization of the USGS reference glasses GSA-1G, GSC-1G, GSD-1G, GSE-1G, BCR-2G, BHVO-2G and BIR-1G using EPMA, ID-TIMS, ID-ICP-MS and LA-ICP-MS. Geostand Geoanal Res 29:285–302. https://doi.org/10.1111/j.1751-908X.2005.tb00901.x

John T, Gussone N, Podladchikov YY, Bebout GE, Dohmen R, Halama R, Klemd R, Magna T, Seitz HM (2012) Volcanic arcs fed by rapid pulsed fluid flow through subducting slabs. Nat Geosci 5:489–492. https://doi.org/10.1038/ngeo1482

Klein E (2003) Geochemistry of the igneous oceanic crust. Treatise Geochem 3:433–463

Konrad-Schmolke M, Halama R (2014) Combined thermodynamic–geochemical modeling in metamorphic geology: boron as tracer of fluid–rock interaction. Lithos 208–209:393–414. https://doi.org/10.1016/j.lithos.2014.09.021

Lanari P, Vidal O, De Andrade V, Dubacq B, Lewin E, Grosch E, Schwartz S (2014) XMapTools: a MATLAB-based program for electron microprobe X-ray image processing and geothermobarometry. Comp Geosci 62:227–240. https://doi.org/10.1016/j.cageo.2013.08.010

Lanari P, Vho A, Bovay T, Airaghi L, Centrella S (2019) Quantitative compositional mapping of mineral phases by electron probe micro-analyser. Geol Soc Lond Spec Publ 478:39–63. https://doi.org/10.1144/SP478.4

Leeman WP, Tonarini S, Chan LH, Borg LE (2004) Boron and lithium isotopic variations in a hot subduction zone—the southern Washington Cascades. Chem Geol 212:101–124. https://doi.org/10.1016/j.chemgeo.2004.08.010

Liu YS, Hu ZC, Gao S, Günther D, Xu J, Gao CG, Chen HH (2008) In situ analysis of major and trace elements of anhydrous minerals by LA-ICP-MS without applying an internal standard. Chem Geol 257:34–43. https://doi.org/10.1016/j.chemgeo.2008.08.004

Liu H, Sun H, Xiao Y, Wang Y, Zeng L, Li W, Guo H, Yu H, Pack A (2019) Lithium isotope systematics of the Sumdo Eclogite, Tibet: Tracing fluid/rock interaction of subducted low-T altered oceanic crust. Geochim Cosmochim Acta 246:385–405. https://doi.org/10.1016/j.gca.2018.12.002

Liu H, Xue YY, Yang T, Jin X, You CF, Lin CT, Sun WD, Deng J (2022) Fluid-rock interactions at shallow depths in subduction zone: Insights from trace elements and B isotopic composition of metabasites from the Mariana forearc. Lithos 422:106730. https://doi.org/10.1016/j.lithos.2022.106730

Luciani N, Nikogosian IK, De Hoog CJ, Davies GR, Koornneef JM (2023) Constraints on crustal recycling from boron isotopes in Italian melt inclusions. Earth Planet Sci Lett 624:118462

Marschall HR, Altherr R, Ludwig T, Kalt A, Gméling K, Kasztovszky Z (2006) Partitioning and budget of Li, Be and B in high-pressure metamorphic rocks. Geochim Cosmochim Acta 70:4750–4769. https://doi.org/10.1016/j.gca.2006.07.006

Marschall HR, Altherr R, Rüpke L (2007a) Squeezing out the slab—modelling the release of Li, Be and B during progressive high-pressure metamorphism. Chem Geol 239:323–335. https://doi.org/10.1016/j.chemgeo.2006.08.008

Marschall HR, von Strandmann PAP, Seitz HM, Elliott T, Niu Y (2007b) The lithium isotopic composition of orogenic eclogites and deep subducted slabs. Earth Planet Sci Lett 262:563–580. https://doi.org/10.1016/j.epsl.2007.08.005

Marschall HR, Wanless VD, Shimizu N, Von Strandmann PAP, Elliott T, Monteleone BD (2017) The boron and lithium isotopic composition of mid-ocean ridge basalts and the mantle. Geochim Cosmochim Acta 207:102–138. https://doi.org/10.1016/j.gca.2017.03.028

Massonne HJ, Schreyer W (1989) Stability field of the high-pressure assemblage, talc + phengite and two new phengite barometers. Eur J Mineral 1:391–410. https://doi.org/10.1127/ejm/1/3/0391

Martin C, Flores KE, Harlow GE (2016) Boron isotopic discrimination for subduction-related serpentinites. Geology 44:899–902. https://doi.org/10.1130/G38102.1

Metcalfe I (2021) Multiple tethyan ocean basins and orogenic belts in Asia. Gondwana Res 100:87–130. https://doi.org/10.1016/j.gr.2021.01.012

Millot R, Guerrot C, Vigier N (2004) Accurate and high-precision measurement of lithium isotopes in two reference materials by MC-ICP-MS. Geostand Geoanal Res 28:153–159. https://doi.org/10.1111/j.1751-908X.2004.tb01052.x

Misra S, Froelich PN (2012) Lithium isotope history of Cenozoic seawater: changes in silicate weathering and reverse weathering. Science 335:818–823. https://doi.org/10.1126/science.1214697

Mposkos E (1989) High-pressure metamorphism in gneisses and pelitic schists in the East Rhodope Zone (N. Greece). Mineral Petrol 41:25–39. https://doi.org/10.1007/BF01164808

Nakano T, Nakamura E (2001) Boron isotope geochemistry of metasedimentary rocks and tourmalines in a subduction zone metamorphic suite. Phys Earth Planet Interiors 127:233–252. https://doi.org/10.1016/S0031-9201(01)00230-8

Nie X, Feng Q, Qian X, Wang Y (2015) Magmatic record of Prototethyan evolution in SW Yunnan, China: geochemical, zircon U-Pb geochronological and Lu–Hf isotopic evidence from the Huimin metavolcanic rocks in the southern Lancangjiang zone. Gondwana Res 28:757–768. https://doi.org/10.1016/j.gr.2014.05.011

Pabst S, Zack T, Savov IP, Ludwig T, Rost D, Vicenzi EP (2011) Evidence for boron incorporation into the serpentine crystal structure. Am Mineral 96:1112–1119. https://doi.org/10.2138/am.2011.3709

Pabst S, Zack T, Savov IP, Ludwig T, Rost D, Tonarini S, Vicenzi EP (2012) The fate of subducted oceanic slabs in the shallow mantle: Insights from boron isotopes and light element composition of metasomatized blueschists from the Mariana forearc. Lithos 132:162–179. https://doi.org/10.1016/j.lithos.2011.11.010

Palmer MR (2017) Boron cycling in subduction zones. Elements 13:237–242. https://doi.org/10.2138/gselements.13.4.237

Paton C, Hellstrom J, Paul B, Woodhead J, Hergt J (2011) Iolite: freeware for the visualisation and processing of mass spectrometric data. J Anal Spectrom 26:2508–2518. https://doi.org/10.1039/C1JA10172B

Peacock SA (1990) Fluid processes in subduction zones. Science 248:329–337. https://doi.org/10.1126/science.248.4953.329

Peacock SM, Hervig RL (1999) Boron isotopic composition of subduction-zone metamorphic rocks. Chem Geol 160:281–290. https://doi.org/10.1016/S0009-2541(99)00103-5

Penniston-Dorland SC, Sorensen SS, Ash RD, Khadke SV (2010) Lithium isotopes as a tracer of fluids in a subduction zone mélange: Franciscan Complex, CA. Earth Planet Sci Lett 292:181–190. https://doi.org/10.1016/j.epsl.2010.01.034

Plank T, Langmuir CH (1993) Tracing trace elements from sediment input to volcanic output at subduction zones. Nature 362:739–743. https://doi.org/10.1038/362739a0

Prelević D, Akal C, Foley SF, Romer RL, Stracke A, Bogaard PVD (2012) Ultrapotassic mafic rocks as geochemical proxies for post-collisional dynamics of orogenic lithospheric mantle: the case of southwestern Anatolia, Turkey. J Petrol 53:1019–1055. https://doi.org/10.1093/petrology/egs008

Qiu L, Rudnick RL, McDonough WF, Merriman RJ (2009) Li and δ^7Li in mudrocks from the British Caledonides: metamorphism and source influences. Geochim Cosmochim Acta 73:7325–7340. https://doi.org/10.1016/j.gca.2009.08.017

Romer RL, Meixner A (2014) Lithium and boron isotopic fractionation in sedimentary rocks during metamorphism—The role of rock composition and protolith mineralogy. Geochim Cosmochim Acta 128:158–177. https://doi.org/10.1016/j.gca.2013.11.032

Romer RL, Meixner A, Hahne K (2014) Lithium and boron isotopic composition of sedimentary rocks—The role of source history

and depositional environment: a 250Ma record from the Cadomian orogeny to the Variscan orogeny. Gondwana Res 26:1093–1110. https://doi.org/10.1016/j.gr.2013.08.015

Rosner M, Erzinger J, Franz G, Trumbull RB (2003) Slab-derived boron isotope signatures in arc volcanic rocks from the Central Andes and evidence for boron isotope fractionation during progressive slab dehydration. Geochem Geophys Geosyst 4:9005. https://doi.org/10.1029/2002GC000438

Rudnick RL, Tomascak PB, Njo HB, Gardner LR (2004) Extreme lithium isotopic fractionation during continental weathering revealed in saprolites from South Carolina. Chem Geol 212:45–57. https://doi.org/10.1016/j.chemgeo.2004.08.008

Savov IP, Ryan JG, D'Antonio M, Kelley K, Mattie P (2005) Geochemistry of serpentinized peridotites from the Mariana Forearc Conical Seamount, ODP Leg 125: Implications for the elemental recycling at subduction zones. Geochem Geophys Geosyst 6:Q04J15. https://doi.org/10.1029/2004GC000777

Savov IP, Ryan JG, D'Antonio M, Fryer P (2007) Shallow slab fluid release across and along the Mariana arc basin system: Insights from geochemistry of serpentinized peridotites from the Mariana fore arc. J. GeophysRes 112:B09205. https://doi.org/10.1029/2006JB004749

Scambelluri M, Tonarini S (2012) Boron isotope evidence for shallow fluid transfer across subduction zones by serpentinized mantle. Geology 40:907–910. https://doi.org/10.1130/G33233.1

Schmidt MW, Vielzeuf D, Auzanneau E (2004) Melting and dissolution of subducting crust at high pressures: the key role of white mica. Earth Planet Sci Lett 228:65–84. https://doi.org/10.1016/j.epsl.2004.09.020

Seitz HM, Woodland AB (2000) The distribution of lithium in peridotitic and pyroxenitic mantle lithologies—An indicator of magmatic and metasomatic processes. Chem Geol 166:47–64. https://doi.org/10.1016/S0009-2541(99)00184-9

Simons KK, Harlow GE, Brueckner HK, Goldstein SL, Sorensen SS, Hemming NG, Langmuir CH (2010) Lithium isotopes in Guatemalan and Franciscan HP–LT rocks: Insights into the role of sediment-derived fluids during subduction. Geochim Cosmochim Acta 74:3621–3641. https://doi.org/10.1016/j.gca.2010.02.033

Smith HJ, Spivack AJ, Staudigel H, Hart SR (1995) The boron isotopic composition of altered oceanic crust. Chem Geol 126:119–135. https://doi.org/10.1016/0009-2541(95)00113-6

Soder CG, Romer RL (2018) Post-collisional potassic–ultrapotassic magmatism of the Variscan orogen: implications for mantle metasomatism during continental subduction. J Petrol 59:1007–1034. https://doi.org/10.1093/petrology/egy053

Spandler C, Hermann J, Faure K, Mavrogenes JA, Arculus RJ (2008) The importance of talc and chlorite "hybrid" rocks for volatile recycling through subduction zones; evidence from the high-pressure subduction mélange of New Caledonia. Contrib Mineral Petrol 155:181–198. https://doi.org/10.1007/s00410-007-0236-2

Spear FS, Cheney JT (1989) A petrogenetic grid for pelitic schists in the system SiO_2-Al_2O_3-FeO-MgO-K_2O-H_2O. Contrib Mineral Petrol 101:149–164. https://doi.org/10.1007/BF00375302

Spivack AJ, Edmond JM (1986) Determination of boron isotope ratios by thermal ionization mass spectrometry of the dicesium metaborate cation. Anal Chem 58:31–35. https://doi.org/10.1021/ac00292a010

Spivack AJ, Edmond JM (1987) Boron isotope exchange between seawater and the oceanic crust. Geochim Cosmochim Acta 51:1033–1043. https://doi.org/10.1016/0016-7037(87)90198-0

Straub SM, Layne GD (2003) Decoupling of fluids and fluid-mobile elements during shallow subduction: evidence from halogen-rich andesite melt inclusions from the Izu arc volcanic front. Geochem Geophys Geosyst. https://doi.org/10.1029/2002GC000349

Sugden PJ, Savov IP, Agostini S, Wilson M, Halama R, Meliksetian K (2020) Boron isotope insights into the origin of subduction signatures in continent-continent collision zone volcanism. Earth Planet Sci Lett 538:116207. https://doi.org/10.1016/j.epsl.2020.116207

Teng FZ, McDonough WF, Rudnick RL, Dalpé C, Tomascak PB, Chappell BW, Gao S (2004) Lithium isotopic composition and concentration of the upper continental crust. Geochim. Cosmochim. Acta 68:4167–4178. https://doi.org/10.1016/j.gca.2004.03.031

Teng FZ, Rudnick RL, McDonough WF, Gao S, Tomascak PB, Liu Y (2008) Lithium isotopic composition and concentration of the deep continental crust. Chem Geol 255:47–59. https://doi.org/10.1016/j.chemgeo.2008.06.009

Tomascak PB (2004) Developments in the understanding and application of lithium isotopes in the earth and planetary sciences. Rev Mineral Geochem 55:153–195. https://doi.org/10.1016/j.chemgeo.2008.06.009

Tomascak PB, Tera F, Helz RT, Walker RJ (1999) The absence of lithium isotope fractionation during basalt differentiation: new measurements by multicollector sector ICP-MS. Geochim Cosmochim Acta 63:907–910. https://doi.org/10.1016/S0016-7037(98)00318-4

Tomascak PB, Ryan JG, Defant MJ (2000) Lithium isotope evidence for light element decoupling in the Panama subarc mantle. Geology 28:507–510. https://doi.org/10.1130/0091-7613(2000)28<507:LIEFLE>3E2.0.CO;2

Tomascak PB, Magna T, Dohmen R (2016) Advances in lithium isotope geochemistry. Springer International Publishing, Cham, pp 1–195. https://doi.org/10.2138/gsrmg.55.1.153

Ueno K, Wang Y, Wang X (2003) Fusulinoidean faunal succession of a Paleo-Tethyan oceanic seamount in the Changning-Menglian Belt, West Yunnan, Southwest China: an overview. Island Arc 12:145–161. https://doi.org/10.1046/j.1440-1738.2003.00387.x

Wang XD, Ueno K, Mizuno Y, Sugiyama T (2001) Late Paleozoic faunal, climatic, and geographic changes in the Baoshan block as a Gondwana-derived continental fragment in southwest China. Palaeogeogr Palaeoclimatol Palaeoecol 170:197–218. https://doi.org/10.1016/S0031-0182(01)00228-0

Wang H, Liu F, Li J, Sun Z, Ji L, Tian Z, Liu L, Santosh M (2019) Petrology, geochemistry and P-T–t path of lawsonite-bearing retrograded eclogites in the Changning-Menglian orogenic belt, southeast Tibetan Plateau. J Metamorph Geol 37:439–478. https://doi.org/10.1111/jmg.12462

Wang D, Romer RL, Guo JH, Glodny J (2020a) Li and B isotopic fingerprint of Archean subduction. Geochim Cosmochim Acta 268:446–466. https://doi.org/10.1016/j.gca.2019.10.021

Wang H, Liu F, Santosh M, Wang F (2020b) Subduction erosion associated with Paleo-Tethys closure: deep subduction of sediments and high pressure metamorphism in the SE Tibetan Plateau. Gondwana Res 82:171–192. https://doi.org/10.1016/j.gr.2020.01.001

Wang H, Liu F, Sun Z, Ji L, Zhu J, Cai J, Zhou K, Li J (2020) A new HP–UHP eclogite belt identified in the southeastern Tibetan Plateau: tracing the extension of the main Palaeo-Tethys suture zone. J Petrol 61:egaa073. https://doi.org/10.1093/petrology/egaa073

Wang H, Liu F, Sun Z, Ji L, Cai J, Zhu J (2021) Identification of continental-type eclogites in the Paleo-Tethyan Changning-Menglian orogenic belt, southeastern Tibetan Plateau: implications for the transition from oceanic to continental subduction. Lithos 396:106215. https://doi.org/10.1016/j.lithos.2021.106215

Wei C, Duan Z (2019) Phase relations in metabasic rocks: constraints from the results of experiments, phase modelling and ACF

analysis. Geol Soc Spec Publ 474:25–45. https://doi.org/10.1144/SP474.10

Whitney DL, Evans BW (2010) Abbreviations for names of rock-forming minerals. Am Mineral 95:185–187. https://doi.org/10.2138/am.2010.3371

Williams LB, Hervig RL, Holloway JR, Hutcheon I (2001) Boron isotope geochemistry during diagenesis. Part I. Experimental determination of fractionation during illitization of smectite. Geochim Cosmochim Acta 65:1769–1782. https://doi.org/10.1016/S0016-7037(01)00557-9

Wu H, Boulter C, Ke B, Stow D, Wang Z (1995) The Changning-Menglian suture zone; a segment of the major Cathaysian-Gondwana divide in Southeast Asia. Tectonophysics 242:267–280. https://doi.org/10.1016/0040-1951(94)00210-Z

Wunder B, Meixner A, Romer RL, Wirth R, Heinrich W (2005) The geochemical cycle of boron: constraints from boron isotope partitioning experiments between mica and fluid. Lithos 84:206–216. https://doi.org/10.1016/j.lithos.2005.02.003

Wunder B, Meixner A, Romer RL, Heinrich W (2006) Temperature-dependent isotopic fractionation of lithium between clinopyroxene and high-pressure hydrous fluids. Contrib Mineral Petrol 151:112–120. https://doi.org/10.1007/s00410-005-0049-0

Wunder B, Meixner A, Romer RL, Feenstra A, Schettler G, Heinrich W (2007) Lithium isotope fractionation between Li-bearing staurolite, Li-mica and aqueous fluids: an experimental study. Chem Geol 238:277–290. https://doi.org/10.1016/j.chemgeo.2006.12.001

Xu R, Romer RL, Glodny J (2021) External fluids cause alteration and metal redistribution in the granite-hosted Tangziwa SnCu deposit, Gejiu district. China Lithos 382:105937. https://doi.org/10.1016/j.lithos.2020.105937

Yamada C, Tsujimori T, Chang Q, Kimura JI (2019) Boron isotope variations of Franciscan serpentinites, northern California. Lithos 334–335:180–189. https://doi.org/10.1016/j.lithos.2019.02.004

Zack T, Tomascak PB, Rudnick RL, Dalpé C, McDonough WF (2003) Extremely light Li in orogenic eclogites: the role of isotope fractionation during dehydration in subducted oceanic crust. Earth Planet Sci Lett 208:279–290. https://doi.org/10.1016/S0012-821X(03)00035-9

Zellmer GF, Edmonds M, Straub SM (2015) Volatiles in subduction zone magmatism. Geol Soc Lond Spec Publ 410:1–17. https://doi.org/10.1144/SP410.13

Zhang XZ, Wang Q, Kerr AC, Wei GJ, Qi Y, Liu Y, Yang YC (2023) Sediment recycling by continental subduction indicated by B-Hf-Pb-Nd isotopes from Miocene-Quaternary lavas in the northern margin of Tibet. Lithos 444:107109. https://doi.org/10.1016/j.lithos.2023.107109

Zheng J, Jin X, Huang H, Zong P (2019) Sedimentology and detrital zircon geochronology of the Nanduan Formation (Carboniferous) of the Changning-Menglian Belt: indications for the evolution of Paleo-Tethys in western Yunnan, China. Int J Earth Sci 108:1029–1048. https://doi.org/10.1007/s00531-019-01694-x

Zheng J, Jin X, Huang H, Yan Z, Wang H, Bai L (2021) Sedimentology and detrital zircon geochronology of the Nanpihe Formation in the central zone of the Changning-Menglian Belt in western Yunnan, China: revealing an allochthon emplaced during the closure of Paleo-Tethys. Int J Earth Sci 110:2685–2704. https://doi.org/10.1007/s00531-021-02074-0